Cryo-EM structure revealed a novel F-actin binding motif in a *Legionella pneumophila* lysine fatty-acyltransferase

Wenjie W. Zeng[a,b], Garrison Komaniecki[c,e], Jiaze Liu,[b,f] Hening Lin[c,d], and Yuxin Mao[a,b,1]

[a]Weill Institute for Cell and Molecular Biology, Cornell University, Ithaca, NY 14853, USA.

[b]Department of Molecular Biology and Genetics, Cornell University, Ithaca, NY 14853, USA.

[c]Department of Chemistry, Department of Molecular Biology and Genetics, Cornell University, Ithaca, NY 14853, USA

[d]Howard Hughes Medical Institute; Department of Medicine and Department of Chemistry, The University of Chicago, Chicago, IL 60637, USA

[e]Current address: Chemistry Department, University of Wisconsin – Parkside, Kenosha, WI 53406, USA.

[f]Current address: Department of Pharmacology, Yale University School of Medicine, New Haven, CT 06520, USA.

[1] Corresponding Author:

E-mail: ym253@cornell.edu

Telephone: 607-255-0783

Abstract

Legionella pneumophila is an opportunistic bacterial pathogen that causes Legionnaires' disease. To establish an intracellular niche conducive to replication, *L. pneumophila* translocates a diverse array of effector proteins that manipulate various host cellular processes, including the actin cytoskeleton. In a screen for effectors that alter actin dynamics, we identified a *Legionella* effector, Lfat1, which colocalizes with the actin cytoskeleton in eukaryotic cells. Lfat1 specifically binds F-actin through a novel actin-binding domain (ABD). High-resolution cryo-electron microscopy (cryoEM) analysis revealed that this ABD forms a long α-helix hairpin, with its tip interacting with subdomains I and II of two adjacent actin molecules within the F-actin filament. Interestingly, while individual α-helices of the hairpin fail to bind F-actin, co-expression as separate fusion proteins restores binding activity. Furthermore, we demonstrated that Lfat1 exhibits lysine fatty-acyltransferase (KFAT) activity, targeting host small GTPases. These findings establish a foundation for studying the KFAT family of bacterial toxins and uncover a novel F-actin binding motif, providing an alternative F-actin marker with notable flexibility.

Introduction

The actin cytoskeleton plays an essential role in diverse cellular processes, including cell motility, cytokinesis, intracellular trafficking, and cell signaling (Dominguez & Holmes, 2011; Letort *et al*, 2015; Pollard, 2016). Actin is one of the most conserved, ubiquitous, and abundant proteins in cells from amoebas to humans (Pollard, 2016). Actin exists in two distinct forms: the monomeric G-actin form and the double-stranded filamentous F-actin form. F-actin is highly dynamic with a net association of ATP-actin to the barbed (+) end and dissociation of ADP-actin monomers from the pointed (-) end (Pollard, 2016). The assembly and disassembly of F-actin *in vivo* is intricately regulated through interactions with a structurally and functionally diverse family of Actin-Binding Proteins (ABPs) (Pollard, 2016). These actin-binding proteins have usually been classified according to their functional properties into several families, such as the actin monomer-binding protein profilin (Carlsson *et al*, 1977); actin nucleators, including Arp2/3 and Formin that initiate *de novo* branched and unbranched filament assembly, respectively (Chen *et al*, 2010; Dong *et al*, 2003; Machesky *et al*, 1994; Pizarro-Cerda *et al*, 2017); the heterodimeric capping proteins that terminate F-actin elongation (Isenberg *et al*, 1980); severing/depolymerization factors Cofilin and Gelsolin (Bamburg *et al*, 1980; Barrie *et al*, 2024; Tanaka *et al*, 2018; Yin & Stossel, 1979); filament binding proteins, such as tropomyosin that binds to the main groove of an actin filament and stabilizes the filament (von der Ecken *et al*, 2015; Yu & Ono, 2006); and cross-linking proteins that crosslink and stabilize multiple F-actin filaments together for cell movement and muscle contraction (Le *et al*, 2017; Ribeiro Ede *et al*, 2014). The accumulation of 3-dimensional structures of ABPs in complex with actin revealed that different ABPs share a limited number of actin-binding structural modules (Van Troys *et al*, 1999). Thus, identifying and characterizing new

59 actin-binding structural modules will provide direct hints of the actin target site and the functional
60 effect on the actin dynamics of ABPs that share the specific actin-binding module.

61 Given actin's essential roles in eukaryotes, many prokaryotic and viral pathogens co-opt a
62 variety of mechanisms that target the host actin cytoskeleton for effective pathogenesis (Aktories
63 *et al*, 2011; Bugalhao *et al*, 2015). The virulence factor BimA from *Burkholderia*
64 *pseudomallei* mimics host actin-polymerizing proteins Ena/VASP to nucleate, elongate, and
65 bundle filaments (Benanti *et al*, 2015). The *Vibrio parahaemolyticus* VopL consists of a VopL C-
66 terminal domain (VCD) and three WASP homology 2 (WH2) motifs and mimics the Arp2/3
67 complex and formin proteins to stimulate actin polymerization (Namgoong *et al*, 2011; Zahm *et*
68 *al*, 2013). The *Salmonella* invasion protein A (SipA) effector is an actin-binding protein that
69 enhances actin polymerization and promotes the uptake efficiency of the bacterium (McGhie *et al*,
70 2004).

71 The gram-negative bacterium *Legionella pneumophila* is the causative agent of a
72 potentially fatal form of pneumonia in humans named Legionnaires' disease (Cunha *et al*, 2016;
73 Fraser *et al*, 1977; McDade *et al*, 1977; Mondino *et al*, 2020). Upon entry into human alveolar
74 macrophage cells, the facultative intracellular pathogen translocates more than 350 different
75 bacterial proteins, known as effectors (Burstein *et al*, 2009; Huang *et al*, 2011; Zhu *et al*, 2011).
76 These effector proteins subvert multiple conserved eukaryotic pathways, such as ubiquitination
77 (Price & Abu Kwaik, 2021; Tomaskovic *et al*, 2022), autophagy (Choy *et al*, 2012; Omotade &
78 Roy, 2020; Thomas *et al*, 2020; Wan *et al*, 2024), lipid metabolism (Hsu *et al*, 2012; Swart &
79 Hilbi, 2020; Toulabi *et al*, 2013), and the actin cytoskeleton (Franco *et al*, 2012; Prashar *et al*,
80 2018; Zhang *et al*, 2023) to aid the pathogen in establishing a *Legionella*-containing vacuole (LCV)

81 amenable to intracellular growth and proliferation (Gomez-Valero *et al*, 2019; Mondino *et al.*,
82 2020; Oliva *et al*, 2018).

83 Like other bacterial pathogens, *L. pneumophila* utilizes a cohort of virulent effectors to
84 modulate actin. Recent studies revealed that the VipA effector nucleates actin and disrupts the
85 Multi-Vesicular Bodies (MVB) pathway (Franco *et al.*, 2012) and the RavK effector cleaves actin
86 to abolish actin polymerization (Liu *et al*, 2017). In our recent screen for *L. pneumophila* effectors
87 that affect host F-actin dynamics, we identified several novel effector proteins that exhibited
88 various degrees of F-actin-associated phenotypes. Among these positive hits, Lpg1387, an effector
89 with no known function, showed strong colocalization with F-actin. In this study, we report the
90 identification of a novel actin-binding motif consisting of a long anti-parallel α-helical hairpin. We
91 further revealed the molecular mechanism of actin-binding by cryo-electron microscopy (cryoEM)
92 and presented evidence for developing a potential F-actin probe based on this novel actin-binding
93 motif. Moreover, using click chemistry, we confirmed that, in addition to the actin-binding motif,
94 Lpg1387 has a lysine fatty-acylate (KFA) catalytic domain specific for small GTPases. Hence, we
95 named this *L. pneumophila* effector Lfat1 (*Legionella F-actin-binding fatty-acyl-transferase 1*).

96 ## Results

97 **The *Legionella* effector Lfat1 directly interacts with F-actin via a coiled-coil domain**

98 To explore how the intracellular bacterial pathogen *Legionella pneumophila* modulates
99 host actin dynamics, we performed a screen to search for effectors that perturb host actin structures.
100 In this screen, we imaged F-actin structures with phalloidin staining in HeLa cells transfected with
101 an GFP-effectors library. In this screen, several effectors showed various degrees of F-actin-
102 associated phenotypes (Figure S1). Among the positive hits, MavH (Lpg2425) has recently been
103 shown to polymerize actin filaments in a membrane-dependent manner (Zhang *et al.*, 2023).
104 Another effector, Lfat1 (Lpg1387), exhibited nearly a complete colocalization with F-actin (Figure
105 S1).

106 To elucidate the molecular mechanism of how Lfat1 localizes to F-actin filaments, we first
107 analyzed the 3-D structure predicted by AlphaFold (Jumper *et al*, 2021). The structure revealed a
108 hammer-like structure for the full-length Lfat1 protein (Figure 1A). The head of the hammer is
109 formed by a globular domain (NC-domain), which is contributed by both the N-terminal (residue
110 1-137, red) and the C-terminal lobes (residues 356-469 pink) of the protein, while the handle of
111 the hammer is formed by an elongated, anti-parallel, coiled-coil hairpin (CC-domain), which
112 contains the middle portion of the protein (residues 138- 355, cyan). To map the region responsible
113 for Lfat1 F-actin localization, we created constructs expressing the NC- and CC-domains fused
114 with an N-terminal GFP, respectively, and investigated their intracellular localization by
115 fluorescence microscopy. Interestingly, while the NC-domain showed a diffused cytosolic
116 localization, the CC-domain exhibited a high colocation to actin filaments comparable to the wild-
117 type protein (Figure 1B and C). This result was further confirmed by an immunoprecipitation (IP)
118 experiment wherein full-length Lfat1 and the CC-domain were able to pulldown actin whereas the

119 NC-domain could not (Figure 1D). To test whether the CC-domain directly binds actin, we
120 performed an *in vitro* F-actin co-sedimentation assay, in which purified recombinant proteins of
121 the CC-domain were incubated with actin in the presence of G-actin or F-actin buffer. Following
122 ultracentrifugation to pellet F-actin, the supernatant and pellet were analyzed on SDS-PAGE
123 (Figure 1E). In the G-actin buffer, both actin and the CC-domain protein remained in the
124 supernatant; however, the CC-domain protein co-sedimented with the polymerized F-actin in the
125 F-actin buffer, indicating that the CC-domain of Lfat1 directly binds to F-actin. Strikingly, when
126 the CC-domain protein was incubated with actin at a 1:1, 1:2, or 1:4 (actin : CC) molar ratio in the
127 F-actin buffer, an approximately equal amount of CC-domain proteins were co-sedimented with
128 F-actin, and the excess CC-domain proteins remained in the supernatant. This observation
129 indicates that the interaction between the CC-domain and actin is saturable, and the binding occurs
130 at a one-to-one molar ratio (Figure 1F). Together, our findings identified Lfat1 as a novel actin-
131 binding effector of *Legionella*. We further demonstrated that Lfat1 binds F-actin at a one-to-one
132 stoichiometry through a unique actin-binding domain (ABD) composed of a long coiled-coil
133 hairpin.

134 **Cryo-EM structure of the Lfat1 ABD-F-actin complex**

135 The discovery of a novel ABD triggered us to interrogate the molecular mechanism of
136 actin-binding by this ABD. We sought to determine the cryo-electron microscopy (cryo-EM)
137 structure of the Lfat1 ABD-F-actin complex. In our initial attempts to prepare the protein complex,
138 F-actin bundles were readily induced by Lfat1 ABD with the F-actin buffer, making it hard to
139 solve a single F-actin filament for structural determination (data not shown). To restrict excessive
140 actin polymerization, equal molar of Lfat1 ABD and G-actin were incubated in a non-polymerizing
141 G-actin buffer overnight at 4°C. The protein complex sample was then applied to cryo-grids,

142 vitrified, and loaded to a 200kV Thermo Fisher Talos Arctica transmission electron microscope
143 for Cryo-EM data collection. The data were processed, and a high-resolution density map (average
144 to 3.5 angstroms resolution) was calculated and refined using CryoSPARC (Punjani *et al*, 2017).
145 The atomic model of the complex was built by docking the F-actin structure (PDB: 7BTI) and the
146 AlphaFold-predicted model of Lfat1 ABD into the CryoEM density using ChimeraX (Meng *et al*,
147 2023). The model was then refined iteratively using Phenix (Liebschner *et al*, 2019), and the final
148 model was validated online by wwPDB validation server at https://validate.wwpdb.org (Figure
149 S2 and Supplemental Table 1).

150 The CryoEM density map of the complex allowed a complete resolution of the actin
151 subunit in the F-actin filament, including its bound ADP and Mg^{2+} ion (Figure 2A, Figure S3A
152 and B). The D-loop (DNase I-binding loop) of the actin monomer adopts a closed conformation.
153 The D-loop of the nth actin monomer extends into the hydrophobic cleft between actin subdomains
154 1 and 3 of the $n+2^{nd}$ actin monomer. The hydrophobic residues (V45, M46, V47, and M49) at the
155 tip of the D-loop pack against a large hydrophobic area aligned the wall of the hydrophobic cleft
156 of the $n+2^{nd}$ actin monomer (Figure 2B). The D-loop also mediates specific hydrogen bond
157 interactions between the two adjacent actin monomers. The main chain amino group of V47 and
158 the carbonyl group of K52 of the D-loop hydrogen bond with the hydroxyl groups of Y145 and
159 Y171, respectively (Figure 2B).

160 The cryo-EM structure also revealed the distal portion of the coiled-coil hairpin, which
161 consists of about 1/3 of the entire Lfat1 ABD domain (Figure S3D). The proximal end of the ABD
162 domain is not visible, likely due to its flexibility, and zeroed out in 2D-class averaging. The
163 structure revealed that the two α-helices of the Lfat1 ABD domain are zipped together by a stretch
164 of hydrophobic residues, mostly leusines and isoleucines (Figure 2C). The ABD domain radiates

165 away from the central F-actin core with its tip of the hairpin region binding to the site between two
166 adjacent actin molecules within each strand of the F-actin filament (Figure 2A). The ABD domain
167 embeds a surface area of 3703 $Å^2$ on the actin filament, which is contributed by both the D-loop
168 region of the nth and the hydrophobic cleft of the $n+2^{nd}$ actin monomers (Figure S4). Several
169 hydrophobic residues (Y240, L241, and L244) located at the tip of the ABD hairpin are
170 accommodated by a hydrophobic pocket formed between the two adjacent actin molecules (Figure
171 2D). The interaction between the ABD domain and the actin filament also involves several
172 hydrogen bonds. The hydroxyl group of Y240 of the ABD domain forms a hydrogen bond with
173 the main chain carbonyl group of V47 at the D-loop; the amino group of D248 of the ABD pairs
174 with the carbonyl oxygen of G48; and the side chain carbonyl oxygen of ABD Q254 makes
175 hydrogen bond with the main chain amine group of S352 of actin. Moreover, salt bridges are also
176 observed between R236 of the ABD domain and D27 and E336 of the $n+2^{nd}$ actin monomer (Figure
177 2D).

178 Together, our cryo-EM structure of the Lfat1 ABD domain in complex with F-actin
179 revealed the intricate molecular basis of multivalent interactions between F-actin and a novel
180 prokaryotic actin-binding domain with a high specificity and affinity. In addition, the complex
181 structure revealed a 1:1 ratio of the interaction between the Lfat1 ABD and actin monomer, which
182 is in agreement with the stoichiometry determined by the previous co-sedimentation experiment
183 (Figure 2A, Figure S3C and D).

184

185 **Validation of key residues on the ABD domain in its recognition of F-actin**

186 To validate our structural observations of the interaction between Lfat1 ABD and F-actin,
187 we performed an alanine substitution mutagenesis experiment of three representative residues
188 (R236, Y240, and Q254) in the Lfat1ABD domain (Figure 3A). We found that GFP-tagged R236A
189 or Q254A ABD mutant showed a slight increase in diffused signals with the majority of proteins
190 remaining colocalized with F-actin. However, the Y240A mutation renders the protein mostly
191 cytosolic (Figures 3B and C). To further validate the fluorescence imaging results, we performed
192 an *in vitro* F-actin co-sedimentation titrating assay to measure the binding affinity between ABD
193 proteins and F-actin (Figure 3D and E). The apparent K_d for wild-type ABD to F-actin is calculated
194 at about 2.7 μM, which is on par with LifeAct (K_d of 2.2 μM) (Riedl *et al*, 2008). Consistently, the
195 K_d for R236A and Q254A mutants increased about 10-fold, 21 and 15 μM, respectively. More
196 strikingly, the Y240A mutant showed a substantial decrease in affinity with a K_d of 245 μM (Figure
197 3D and E). In summary, the mutagenesis experiments confirmed that multivalent interactions
198 contribute to the binding of Lfat1 ABD with F-actin with hydrophobic interactions playing a
199 central role, and the affinity and specificity were further enhanced by hydrogen bond and salt
200 bridge interactions.

201

202 **Comparison of Lfat1 ABD with other actin-binding domains**

203 The discovery of a novel ABD from the *Legionella* effector Lfat1 prompted us to compare
204 this unique ABD to other representative actin-binding proteins. Although ABDs adopt a diverse
205 structural fold, most of them share a similar interaction scheme with F-actin by targeting a hotspot
206 encompassing the D-Loop of $Actin_n$ and the hydrophobic cleft of $Actin_{n+2}$ (Figure 4A and B)
207 (Dominguez, 2004). For example, LifeAct, which is derived from the first 17 residues from
208 *Saccharomyces cerevisiae* ABP140 (Riedl *et al.*, 2008), utilizes the hydrophobic residues aligned

209 on one side of its amphipathic α-helix to engage primarily hydrophobic interactions with a small
210 hydrophobic patch at the F-actin hotspot (Belyy *et al*, 2020; Kumari *et al*, 2020). The actin-binding
211 CH1 domain of Utrophin (a neuromuscular junction scaffolding protein) contains multiple F-actin
212 binding sites (Keep, 2000; Keep *et al*, 1999). Two of the actin-binding sites on the CH1 domain
213 interact primarily with the D-loop region of the nth actin monomer, and the third one, consisting of
214 the N-terminal α-helix, spills the interface further into the subdomain I region of the nth actin
215 subunit (Kumari *et al.*, 2020). The *Pseudomonas aeruginosa* effector protein, Exotoxin Y or ExoY,
216 uses its C-terminal "anchor" helix to engage primarily hydrophobic interactions with the
217 hydrophobic cleft in subdomain 1 of the $n+2^{nd}$ actin subunit (Belyy *et al*, 2021) in a way similar
218 to that of LifeAct (Belyy *et al.*, 2020). ExoY also contains a peptide, which meanders on the
219 surface of the $n+2^{nd}$ actin subunit and functions as a "sensor" for the actin activator but contributes
220 little affinity to F-actin binding (Belyy *et al.*, 2021). These examples support that the hydrophobic
221 cleft formed by subdomain 1 and 3 is the "hotspot" for many ABDs, and the binding site on actin
222 is frequently extended to the vicinity of the "hotspot" depending on unique features associated
223 with each ABD (Figure 4A).

224 A structural comparison of the ABD-F-actin complex structures also revealed that the actin
225 D-loop adopts a variety of conformations upon the binding of different ABDs (Figure 4B). In
226 globular G-actin, the D-Loop is either disordered or adopts an α-helix, depending on its nucleotide
227 state or binding with G-actin binding proteins (Graceffa & Dominguez, 2003). In F-actin, the D-
228 Loop inserts itself into the hydrophobic target-binding cleft of the n+2 subunit immediately above
229 it (Das *et al*, 2020; Dominguez & Holmes, 2011). The D-loop region is also involved in direct
230 interactions with many ABDs (Figure 4). In the Lfat1 ABD and F-actin complex, specific
231 hydrogen bonds are formed between the backbone carbonyl group of D-loop residues V47 and

232 G48 and the ABD residues Y240 and D248 (Figure 2D). These hydrogen bonding interactions
233 cause the D-loop to insert slightly deeper into the hydrophobic cleft and induce a unique
234 conformation of the D-loop residues G50 and Q51 (*Bos taurus* numbering, equivalent to G48 and
235 Q49 in *G. gallus*) not observed in other structures (Figure 4B). This observation suggests that
236 although the hydrophobicity of the "hotspot" plays a dominant role in ABD-binding, the capacity
237 to accommodate the large variety of actin-binding motifs at the "hot spot" is likely due to the
238 structural plasticity of the D-loop.

239

240 **Engineering novel F-actin probes derived from the Lfat1 ABD**

241 Fluorescent toxins or proteins are frequently used as F-actin probes in fixed or live cells,
242 however, they all have certain limitations (Belin *et al*, 2014; Courtemanche *et al*, 2016; Lemieux
243 *et al*, 2014; Munsie *et al*, 2009). The discovery of a new F-actin binding domain from the
244 *Legionella* effector Lfat1 inspired us to investigate whether it can be developed as an alternative
245 *in vivo* F-actin probe. We first tried to map the minimum F-actin binding region in Lfat1 ABD. A
246 series of ABD truncations: ABD-S1 (residues 171-323), ABD-S2 (190-306), and ABD-S3 (211-
247 280) were created and transiently expressed in Hela cells. All three truncated versions
248 demonstrated specific colocalization with F-Actin comparable to the full-length ABD (Figure 5A).
249 However, further shortening of this ABD resulted in loss of function and exhibited a complete
250 cytosolic location (data not shown). Thus, our studies revealed a novel F-actin probe consisting of
251 a 70 amino acid-long alpha-helix hairpin.

252 The Lfat1 ABD contains two long alpha helixes forming a hairpin. We next asked whether
253 this ABD remains functional if the alpha-helix hairpin is split into two individual alpha helixes.

254 To test this, we fused an N-terminal mCherry with α1 and a C-terminal GFP with the α2 of the
255 ABD, respectively, and examined their intracellular localization. All these single alpha helix
256 fusions showed a diffused localization (Figure S5A, B), however, to our surprise, when the two
257 fusion constructs encoding full-length ABD-α1 and α2 were expressed together, these two alpha
258 helixes were able to form a functional ABD and colocalized with F-Actin as the intact wild type
259 ABD (Figure 5C and D). Interestingly, the alpha helixes derived from ABD-S1 could also
260 reconstitute a functional F-actin probe, but not the further shortened alpha helices derived from
261 ABD-S2 (Figures 5C and D). These results suggested that the F-actin probe derived from the Lfat1
262 ABD can be used in a split form, providing flexibility to this new probe.

263

264 **Lfat1 is a lysine fatty acyltransferase (KFAT)**

265 The AlphaFold-predicted structure of Lfat1 revealed a globular domain composed of the
266 N- and C-terminus beside the central, coiled-coil hairpin (Figure 1A). Structural homology search
267 using the DALI server (Holm & Rosenstrom, 2010) yielded the top hit as the RID (Rho GTPase
268 Inactivation Domain) toxin from the *Vibrio vulnificus* (PDB:5XN7) with a Z-score of 7.9. The
269 catalytic domain of both proteins contains a central β-sheet flanked by multiple α helices. The
270 conserved catalytic dyads (H38 and C403) in Lfat1 were positioned with a similar orientation to
271 the dyads in the RID toxin (H2595 and C2835) (Figure 6A).

272 The RID toxin is a lysine fatty acyltransferase (KFAT) processed from a much larger
273 prototoxin that transfers long acyl chains to the ε-amine of lysines in small GTPases, such as those
274 in the Rac subfamily (Zhou *et al*, 2017). To determine whether Lfat1 possesses a similar KFAT
275 activity, we probed the fatty acylation of a small GTPase Rac3. Briefly, HEK-293T cells were co-

276 transfected with plasmids expressing Flag-Rac3 and GFP-Lfat1 or its catalytic mutants followed
277 by treatment with Alk14, a clickable chemical analog of palmitic acid modified with a terminal
278 alkyne moiety. Flag-Rac3 proteins were enriched from transfected cells by immunoprecipitation
279 and were then conjugated to an azide-containing fluorophore, TAMRA-N_3 via copper-catalyzed
280 cycloaddition (Hein *et al*, 2008). The reaction products were separated by SDS-PAGE and
281 analyzed by in-gel fluorescence detection and Western blot. Robust fluorescence signals
282 associated with Rac3 were detected in the presence of wild-type Lfat1, but not its H38A or C403A
283 catalytic mutants (Figure 6B). Furthermore, we found that Rac3-associated fluorescence signals
284 were stable even after the hydroxylamine (HA) treatment, which can reverse acylation on cysteine
285 but not lysine residues. We next asked whether Lfat1 can fattyacylate other host targets. To address
286 this question, we performed a click chemistry-coupled SILAC (Stable Isotope Labeling by Amino
287 Acids in Cell Culture) mass-spectrometry experiment to identify potential targets (Figure S6A).
288 Interestingly, nearly half of the top hits are small GTPases, including Rabs, RheB, RalA, and
289 Rap1B (Figure S6B). Fattyacylation by Lfat1 on several of the small GTPases was further verified
290 using click chemistry (Figure S6C-F). Together, our results demonstrated that the *Legionella*
291 effector Lfat1 is a *bona fide* KFAT that potentially fattyacylates host small GTPases when
292 exogenously expressed in cultured cells.

Discussion

In this study, we identified a novel actin-binding domain from *Leginella pneumophila*. This prokaryote-originated ABD has an alpha-helical hairpin-like structure, which is unprecedented from any other known ABDs. We further mapped the minimum region (~ 70 residues) required for actin binding and demonstrated the feasibility of using this prokaryote ABD as an alternative F-actin probe. Another unique and potentially useful characteristic of this probe is its ability to function as a split-ABD. Although the individual alpha helix derived from the Lfat1 ABD fails to bind actin, they were able to reconstitute a functional intact ABD when co-expressed. This unique feature can be harnessed to target multi-component biological complexes to F-actin by genetically fusing individual components to the split alpha helixes. Furthermore, our cryo-EM structure revealed that the Lfat1 ABD intersects with F-actin obliquely. Its N- and C-termini are pointed away with an adjustable distance from the filament depending on the size of the designed ABD. Thus, the Lfat1 ABD can be used to target proteins of interest to F-actin with a tunable distance from the filament to achieve spatial distribution-related specificity.

F-actin probes are essential tools in cell biology for visualizing and studying the dynamics of the actin cytoskeleton in living and fixed cells. These probes come in various forms, including fluorescently labeled phalloidins, actin-binding proteins, and genetically encoded fluorescent actin markers (Melak *et al*, 2017). Each type of probe has its advantages and limitations. The choice of probe depends on the specific experimental requirements, such as whether live-cell imaging is needed, the level of perturbation that can be tolerated, and the ease of use. The toxic chemical derived from fungi, phalloidin, has been developed as the gold standard F-actin marker to stain actin in fixed samples and tissues (Cooper, 1987). However, it is not suitable for live-cell imaging due to its toxicity and low cell permeability. Many yeast- or human-derived actin-binding domains

316 have been developed into F-actin probes by fusion with fluorescent proteins. Lifeact (Riedl *et al.*,
317 2008), utrophin (Burkel *et al*, 2007), and F-tractin (Brehm *et al*, 2004) are the three most
318 commonly used genetically encoded probes. Although these probes have been widely used for
319 live-cell imaging, they suffer from problems such as low affinity for F-actin and perturbation in
320 actin dynamics. Our discovery of a novel ABD offers an alternative F-actin probe that not only
321 can be used to study actin dynamics but also can be used to as a versatile anchor to target specific
322 activities to F-actin.

323 Our finding that Lfat1 is a protein lysine fatty acyl transferase provides important insights
324 to understand the physiolical function of Lfat1. The Rho Inactivation Domain (RID) is a module
325 found in Multifunctional-Autoprocessing Repeats-in-Toxin (MARTX) toxins produced by certain
326 Gram-negative pathogenic bacteria, such as *Vibrio cholerae* and *Vibrio vulnificus* (Satchell, 2015).
327 RID primarily targets the Rho GTPase family members by the covalent attachment of long-chain
328 fatty acids to the ε-amino groups of lysine residues. The modification inactivates the small
329 GTPases, leading to disruption of the actin cytoskeleton and consequent cell rounding and hence
330 facilitating bacterial invasion and impairing host immune responses (Zhou *et al.*, 2017). A recent
331 study reported that RID modifies other host proteins, notably septins. Fatty-acylation on septins
332 alters the localization and compromises the host cell structural integrity (Xu *et al*, 2024). In this
333 study, we demonstrated that the globular NC-domain of Lfat1 is a *bona fide* KFAT. Using Click
334 chemistry, we showed that Lfat1 could fatty-acylate lysines of the host small GTPase Rac3 (Figure
335 6B) and other small GTPases (Figure S6). We believe that Lfat1 is confined to F-actin through its
336 ABD domain upon secretion from the bacterium, thereby providing substrate specificity for
337 modifying host targets near F-actin structures. Indeed, many of the small GTPase substrates we
338 identified, are known to associate with and regulating actin. For example, RhoG regulates the actin

339 cytoskeleton in lymphocytes (Vigorito *et al*, 2003); Rap1 is reported to regulate actin
340 reorganization and microtuble organizing center polarization at the B cell immune synapse (Wang
341 *et al*, 2017); RheB is reported to regulate actin filament distribution (Gau *et al*, 2005); Ral GTPases
342 (RalA and RalB) links Ras, Rac, Rho signaling to control cell migration (Zago *et al*, 2019); and
343 RAB8A regulates spindle migration via ROCK-mediated actin assembly in mouse oocyte meiosis
344 (Pan *et al*, 2019). The identification of the KFAT effectors among all *Legionella* species and set
345 up a solid foundation for further characterizations of this family of effectors. However, future
346 studies will be needed to identify which substrates are physiologicaly important under infection
347 conditions.

Acknowledgments

We thank Dr. Sheng Zhang and Dr. Qin Fu for helping with the proteomics study. W.Z. acknowledges support from the T32 training grant and the Sadov Graduate Student Fellowship (Cornell University). This work is supported by the National Institutes of Health R01GM144452(Y.M.), R01AI153110 (H.L.), and HHMI.

354 **Material and methods**

355 **Plasmid construction**

356 Please refer to Supplemental Table 2 for constructs used in this study. All targeted DNA
357 fragments were amplified by PCR using the primers listed in Supplemental Table 3. The amplified
358 DNA fragments were digested by restriction enzymes, BamHI and XhoI, and ligated to
359 corresponding vector plasmids. Plasmids containing the targeted genes were amplified using
360 NEB® Stable Competent C3040I *E. coli* strain and verified by sequencing. For mutagenesis,
361 plasmids containing wild-type genes were used as templates with mutagenic primers in a PrimeStar
362 MasterMix PCR reaction to amplify the entire plasmid, followed by DpnI digestion, and plasmids
363 carrying the desired mutations were amplified using the C3040I *E. coli* strain and verified by
364 sequencing.

365

366 **Protein purification**

367 Actin was purified from muscle acetone powder prepared from ground beef (Pardee &
368 Spudich, 1982). Briefly, 10 grams of muscle acetone powder was dissolved with 200 ml G-actin
369 buffer (5 mM Tris pH 7.5, 0.2 mM $CaCl_2$, 0.2 mM ATP, 0.5 mM DTT) at 4 ºC with stirring for 30
370 minutes followed by low-speed centrifugation at 5000-10,000g for 10-20 minutes to remove
371 insoluble solids. Soluble extracts were centrifuged at 15,000g for 60 min at 4 ºC, and actin was
372 precipitated by the slow addition of solid ammonium sulfate to reach 25% saturation. Precipitates
373 were collected by centrifugation at 15,000g for 30 min and dissolved in 50 ml G-actin buffer and
374 dialyzed against 2 liters of G-actin buffer overnight with two changes of buffer. The dialyzed actin
375 solution was centrifuged at 32,000g for 60 min to remove any aggregates. Actin was polymerized

376 by the addition of 10x polymerization buffer to a final solution containing 150 mM KCl, 2 mM
377 $MgCl_2$, 2 mM EGTA, and 1 mM ATP. Polymerization was allowed to proceed for 30 min at 25 °C,
378 then in a cold room for 90 min. F-actin was pelleted by centrifugating at 100,000g for 30 min, and
379 the pellet was resuspended in 10–20 ml G-actin buffer and homogenized in a glass-glass
380 homogenizer on ice. The suspension was dialyzed against 2 liters of G-actin buffer for 48 hours
381 with four changes of dialysis solution to completely depolymerize the F-actin. The solution was
382 further clarified by centrifugation at 32,000g for 60 min. The clarified supernatant was loaded onto
383 a Sephadex G-150 or Sephacryl S-100 HR column, equilibrated in G-actin buffer, to remove the
384 remaining contaminating G-actin-binding proteins. Peak fractions were analyzed by SDS- PAGE,
385 pooled, and flash-frozen in liquid nitrogen before storage.

386 Recombinant Lfat1 ABD (WT and mutants) proteins were expressed in Rosetta *E. coli*.
387 The expression was induced by 0.1 mM IPTG at 18 ºC overnight. The bacteria were harvested by
388 centrifugation at 4,000 RPM for 20 minutes. The cell pellets were lysed in Buffer A (20 mM Tris
389 pH7.5, 150 mM NaCl) using sonication. The whole cell lysate was then centrifuged at 16,000 RPM
390 for 40 minutes at 4 ºC, and the clarified lysate was then bound to Cobalt resins on a rotator at 4 ºC
391 for 2 hours. The resins were then extensively washed with Buffer A, and the ABD proteins were
392 released from the resin by a SUMO-specific protease, Ulp1. The released proteins were collected
393 and further purified using size-exclusion chromatography on a Superdex S75 column. The purified
394 ABD proteins were concentrated and then flash-frozen in liquid nitrogen for storage.

395

396 **Cell culture and co-immunoprecipitation**

397 HEK293T and HeLa cells were maintained at a low passage and grown in DMEM
398 (Dulbecco's Modified Eagle Medium) supplemented with 10% FBS (fetal bovine sera). For
399 transfection, plasmids were mixed with 1 mg/ml PEI (polyethylenimine MW10K, Millipore Sigma)
400 at a 5:1 ratio in DMEM incubated for 15 minutes at room temperature, and added directly to cells.
401 After 24 hours of transfection, the cells were used either for immunoprecipitation or imaging
402 experiments.

403 For immunoprecipitation, HEK293T cells transfected with the indicated plasmids after 24
404 hours were chilled on ice, washed with ice-cold PBS, and detached using lysis buffer (20 mM Tris
405 pH7.5, 150 mM NaCl, 1 mM DTT, 0.5% Triton X-100, 0.1% sodium deoxycholate, 1 mM PMSF,
406 with Roche protease inhibitor cocktail). The cells were then lysed using a sonicator on ice. The
407 lysate was clarified by centrifugation at 16,000 RPM for 15 minutes at 4 ºC. The lysate was then
408 incubated with anti-GFP nanobody beads for 2 hours with rotating. The mixture was then washed
409 in a buffer containing 20 mM Tris pH7.5, 150 mM NaCl, 1 mM DTT, and 0.5% Triton X-100.
410 The washed beads were then dissolved in 1X SDS loading buffer, and the samples were analyzed
411 by SDS-PAGE followed by Western-blot and scanned using Li-COR Odyssey CLx scanner.

412

413 **Fluorescence Microscopy**

414 HeLa cells grown on glass cover slides were transfected with the indicated plasmids after
415 24 hours. The cells were then washed with PBS and fixed in 4% PFA in PBS for 15 minutes at
416 room temperature. The fixed cells were washed twice with PBS and incubated with Odyssey
417 blocking buffer with 0.1% saponin and rhodamine- or CF647-phalloidin (Thermofisher) for 1 hour
418 at room temperature. The stained cells were washed three times with PBS and mounted on a glass

419 specimen slide with Fluoromount-G (Thermofisher), and were imaged using a 3i spinning-disc
420 confocal fluorescence microscope. Line-scan analysis was performed using ImageJ (Schneider *et*
421 *al*, 2012).

422

423 **CryoEM sample preparation, data collection, data processing**

424 Purified G-actin (1 mg/ml) was mixed with an equal molar of ABD in G-actin buffer and
425 incubated overnight at 4 ºC. The ABD-F-actin complex samples with a serial dilution were applied
426 to a glow-discharged copper Quantifoil r1.2/1.3 grids and rapidly plunged frozen in liquid ethane
427 using FEI-Vitrobot-Mark-IV. The vitrified grids were then transferred to liquid nitrogen for
428 storage and data collection.

429 For data collection, the grids were imaged using a ThermoFisher Talos Arctica 200 kV
430 electron microscope with a K3 direct electron detector and a Gatan bioquantum energy filter and
431 the dataset was collected using SerialEM software using the following parameters: -0.4 to -3.0 µm
432 defocus range, pixel size of 1.5879062 Å, total electron dose of 40.68 electrons per $Å^2$, exposure
433 time of 1.23 seconds, 50 frames per movie, and 4548 total movies. The movies were then imported
434 into CryoSPARC (Punjani *et al.*, 2017) for motion correction and patch-CTF estimation. 2173 out
435 of 4548 micrographs were selected after manual curation. The CryoSPARC Helical Tracer job
436 was utilized to perform particle picking with a minimum particle diameter of 50 Å and a maximum
437 diameter of 100 Å, with each particle separated by 100 Å. A total of 1,733,108 particles were
438 extracted from micrographs using a box size of 480 pixels. Iterative 2D classifications were
439 performed on these particles, and low-resolution classes were discarded after each iteration.

440 Finally, 1,220,462 particles were used for ab-initio initial model building, followed by iterative
441 helical and local refinements.

442

443 **Model building, refinement, validation**

444 The atomic model of F-actin (PDB: 7BTI) and the AlphaFold-predicted model of
445 Lfat1ABD were docked into the finalized CryoEM density using ChimeraX 1.25 (Pettersen *et al*,
446 2021). The atomic model of the F-actin-ABD complex was then refined iteratively using Phenix
447 (Adams *et al*, 2010), and the final model, CryoEM full-map and half-maps, were validated by the
448 Worldwide Protein Data Bank (wwPDB).

449

450 **F-actin co-sedimentation assay**

451 Recombinant Lfat1 ABD was mixed with buffer control or G-actin at a final concentration
452 of 20 μM. The mixed samples were either incubated in G-actin buffer or F-actin polymerization
453 buffer (50 mM KCl, 2 mM MgCl2) at room temperature for 30 minutes followed by centrifugation
454 at 70,000 RPM for 30 minutes at 4 ºC. The supernatant and pellet were then analyzed on SDS-
455 PAGE.

456 To determine the F-actin binding affinity of ABD, purified recombinant Lfat1 ABD WT
457 and mutant proteins were diluted in G-actin buffer in a series of concentration at 0, 1.25, 2.5, 5,
458 7.5, 10, 15, 20, 30, 40, 50, 60 μM and were incubated with 20 μM of G-actin. Actin polymerization
459 was initiated at room temperature for 30 minutes by adding F-actin polymerization buffer. The
460 samples were then centrifugated at 70,000 RPM for 30 minutes at 4 ºC, and the supernatants and

461 pellets were then analyzed on SDS-PAGE and staining Coomas Brilliant Blue dye, and the
462 intensity of the bands was quantified using ImageJ. and the intensity of the ABD band was divided
463 by the intensity of the actin band in the pellet fractions to calculate the % of ABD bound to F-actin.
464 The average of each data point from three independent experiments was then plotted, and an
465 exponential fit was used to calculate the apparent K_d in R studio.

466

467 **Protein fatty-acylation detection via Click chemistry**

468 Indicated plasmids were transfected into HEK 293T cells using PEI transfection reagent.
469 After overnight transfection, cells were treated with 50 μM Alk14 (Cayman Chemical) for 6 hours.
470 The cells were washed with ice-cold PBS and then lysed in lysis buffer (25 mM Tris-HCl, pH 7.8,
471 150 mM NaCl, 10% glycerol, and 1% NP-40) with protease inhibitor cocktail at 4 °C for 30 min.
472 After centrifugation at 17,000 g for 30 min at 4 ºC, the supernatant was collected and incubated
473 with 20 μL of anti-Flag affinity beads (Sigma Aldrich) at 4 °C for 2 h. The affinity beads was
474 washed three times with washing buffer (25 mM Tris-HCl, pH 7.8, 150 mM NaCl, 0.2% NP-40)
475 and resuspended in 20 μL of washing buffer. TAMRA-N3 (Lumiprobe), TBTA (TCI chemicals),
476 $CuSO_4$, and TCEP (Millipore) were added into the reaction mixture in the order listed. The click
477 chemistry reaction was allowed to proceed at room temperature for 30 min. The reaction was
478 quenched by adding 6x SDS loading dye and boiled for 5 min. Where indicated, samples were
479 treated with hydroxylamine (HA) to remove cysteine fatty acylation. The samples were then
480 separated on SDS-PAGE and fixed in a buffer (50% CH_3OH, 40% water and 10% acetic acid) by
481 shaking for 1 hours at 4ºC and then washed and store in water. The gel was scanned to record
482 fluorescence signal using a ChemiDoc MP (BioRad).

483

484 **SILAC sample preparation and MS data analysis**

485 SILAC samples were prepared from cells transiently expressing WT or H38A mutant Lfat1
486 using a published protocol (Kosciuk *et al*, 2020). The samples were then trypsin digested and the
487 peptides were analyzed using an Orbitrap Fusion™ Tribrid™ (Thermo-Fisher Scientific) mass
488 spectrometer. The MS and MS/MS spectra were subjected to database searches using Proteome
489 Discoverer (PD) 2.4 software (Thermo Fisher Scientific, Bremen, Germany) with the Sequest HT
490 algorithm. The database search was conducted against a *Homo sapiens* Uniprot database with the
491 following variable modifications: methionine oxidation; deamidation of asparagine/glutamine;
492 SILAC heavy: R10 (10.008 Da) and K8 (8.014 Da) and light labeling on R and K; palmitoylation
493 plus biotin on K, protein N-terminus and fixed modification of cysteine carbamidomethylation.

494

495 **References**

496

497 Adams PD, Afonine PV, Bunkoczi G, Chen VB, Davis IW, Echols N, Headd JJ, Hung LW, Kapral GJ, Grosse-
498 Kunstleve RW *et al* (2010) PHENIX: a comprehensive Python-based system for macromolecular
499 structure solution. *Acta Crystallogr D Biol Crystallogr* 66: 213-221
500 Aktories K, Lang AE, Schwan C, Mannherz HG (2011) Actin as target for modification by bacterial protein
501 toxins. *FEBS J* 278: 4526-4543
502 Bamburg JR, Harris HE, Weeds AG (1980) Partial purification and characterization of an actin
503 depolymerizing factor from brain. *FEBS Lett* 121: 178-182
504 Barrie KR, Rebowski G, Dominguez R (2024) Mechanism of actin filament severing and capping by gelsolin.
505 *Nat Struct Mol Biol*
506 Belin BJ, Goins LM, Mullins RD (2014) Comparative analysis of tools for live cell imaging of actin network
507 architecture. *Bioarchitecture* 4: 189-202
508 Belyy A, Merino F, Mechold U, Raunser S (2021) Mechanism of actin-dependent activation of nucleotidyl
509 cyclase toxins from bacterial human pathogens. *Nat Commun* 12: 6628
510 Belyy A, Merino F, Sitsel O, Raunser S (2020) Structure of the Lifeact-F-actin complex. *PLoS Biol* 18:
511 e3000925
512 Benanti EL, Nguyen CM, Welch MD (2015) Virulent Burkholderia species mimic host actin polymerases to
513 drive actin-based motility. *Cell* 161: 348-360
514 Brehm MA, Schreiber I, Bertsch U, Wegner A, Mayr GW (2004) Identification of the actin-binding domain
515 of Ins(1,4,5)P3 3-kinase isoform B (IP3K-B). *Biochem J* 382: 353-362
516 Bugalhao JN, Mota LJ, Franco IS (2015) Bacterial nucleators: actin' on actin. *Pathog Dis* 73: ftv078
517 Burkel BM, von Dassow G, Bement WM (2007) Versatile fluorescent probes for actin filaments based on
518 the actin-binding domain of utrophin. *Cell Motil Cytoskeleton* 64: 822-832
519 Burstein D, Zusman T, Degtyar E, Viner R, Segal G, Pupko T (2009) Genome-scale identification of
520 Legionella pneumophila effectors using a machine learning approach. *PLoS Pathog* 5: e1000508
521 Carlsson L, Nystrom LE, Sundkvist I, Markey F, Lindberg U (1977) Actin polymerizability is influenced by
522 profilin, a low molecular weight protein in non-muscle cells. *J Mol Biol* 115: 465-483
523 Chen Z, Borek D, Padrick SB, Gomez TS, Metlagel Z, Ismail AM, Umetani J, Billadeau DD, Otwinowski Z,
524 Rosen MK (2010) Structure and control of the actin regulatory WAVE complex. *Nature* 468: 533-538
525 Choy A, Dancourt J, Mugo B, O'Connor TJ, Isberg RR, Melia TJ, Roy CR (2012) The Legionella effector RavZ
526 inhibits host autophagy through irreversible Atg8 deconjugation. *Science* 338: 1072-1076
527 Cooper JA (1987) Effects of cytochalasin and phalloidin on actin. *J Cell Biol* 105: 1473-1478
528 Courtemanche N, Pollard TD, Chen Q (2016) Avoiding artefacts when counting polymerized actin in live
529 cells with LifeAct fused to fluorescent proteins. *Nat Cell Biol* 18: 676-683
530 Cunha BA, Burillo A, Bouza E (2016) Legionnaires' disease. *Lancet* 387: 376-385
531 Das S, Ge P, Oztug Durer ZA, Grintsevich EE, Zhou ZH, Reisler E (2020) D-loop Dynamics and Near-Atomic-
532 Resolution Cryo-EM Structure of Phalloidin-Bound F-Actin. *Structure* 28: 586-593 e583
533 Dominguez R (2004) Actin-binding proteins--a unifying hypothesis. *Trends Biochem Sci* 29: 572-578
534 Dominguez R, Holmes KC (2011) Actin structure and function. *Annu Rev Biophys* 40: 169-186
535 Dong Y, Pruyne D, Bretscher A (2003) Formin-dependent actin assembly is regulated by distinct modes of
536 Rho signaling in yeast. *J Cell Biol* 161: 1081-1092
537 Franco IS, Shohdy N, Shuman HA (2012) The Legionella pneumophila effector VipA is an actin nucleator
538 that alters host cell organelle trafficking. *PLoS Pathog* 8: e1002546
539 Fraser DW, Tsai TR, Orenstein W, Parkin WE, Beecham HJ, Sharrar RG, Harris J, Mallison GF, Martin SM,
540 McDade JE *et al* (1977) Legionnaires' disease: description of an epidemic of pneumonia. *N Engl J Med*
541 297: 1189-1197

542 Gau CL, Kato-Stankiewicz J, Jiang C, Miyamoto S, Guo L, Tamanoi F (2005) Farnesyltransferase inhibitors
543 reverse altered growth and distribution of actin filaments in Tsc-deficient cells via inhibition of both
544 rapamycin-sensitive and -insensitive pathways. *Mol Cancer Ther* 4: 918-926
545 Gomez-Valero L, Rusniok C, Carson D, Mondino S, Perez-Cobas AE, Rolando M, Pasricha S, Reuter S,
546 Demirtas J, Crumbach J *et al* (2019) More than 18,000 effectors in the Legionella genus genome
547 provide multiple, independent combinations for replication in human cells. *Proc Natl Acad Sci U S A*
548 116: 2265-2273
549 Graceffa P, Dominguez R (2003) Crystal structure of monomeric actin in the ATP state. Structural basis of
550 nucleotide-dependent actin dynamics. *J Biol Chem* 278: 34172-34180
551 Hein CD, Liu XM, Wang D (2008) Click chemistry, a powerful tool for pharmaceutical sciences. *Pharm Res*
552 25: 2216-2230
553 Holm L, Rosenstrom P (2010) Dali server: conservation mapping in 3D. *Nucleic Acids Res* 38: W545-549
554 Hsu F, Zhu W, Brennan L, Tao L, Luo ZQ, Mao Y (2012) Structural basis for substrate recognition by a unique
555 Legionella phosphoinositide phosphatase. *Proc Natl Acad Sci U S A* 109: 13567-13572
556 Huang L, Boyd D, Amyot WM, Hempstead AD, Luo ZQ, O'Connor TJ, Chen C, Machner M, Montminy T,
557 Isberg RR (2011) The E Block motif is associated with Legionella pneumophila translocated substrates.
558 *Cell Microbiol* 13: 227-245
559 Isenberg G, Aebi U, Pollard TD (1980) An actin-binding protein from Acanthamoeba regulates actin
560 filament polymerization and interactions. *Nature* 288: 455-459
561 Jumper J, Evans R, Pritzel A, Green T, Figurnov M, Ronneberger O, Tunyasuvunakool K, Bates R, Zidek A,
562 Potapenko A *et al* (2021) Highly accurate protein structure prediction with AlphaFold. *Nature* 596:
563 583-589
564 Keep NH (2000) Structural comparison of actin binding in utrophin and dystrophin. *Neurol Sci* 21: S929-
565 937
566 Keep NH, Winder SJ, Moores CA, Walke S, Norwood FL, Kendrick-Jones J (1999) Crystal structure of the
567 actin-binding region of utrophin reveals a head-to-tail dimer. *Structure* 7: 1539-1546
568 Kosciuk T, Price IR, Zhang X, Zhu C, Johnson KN, Zhang S, Halaby SL, Komaniecki GP, Yang M, DeHart CJ *et*
569 *al* (2020) NMT1 and NMT2 are lysine myristoyltransferases regulating the ARF6 GTPase cycle. *Nat*
570 *Commun* 11: 1067
571 Kumari A, Kesarwani S, Javoor MG, Vinothkumar KR, Sirajuddin M (2020) Structural insights into actin
572 filament recognition by commonly used cellular actin markers. *EMBO J* 39: e104006
573 Le S, Hu X, Yao M, Chen H, Yu M, Xu X, Nakazawa N, Margadant FM, Sheetz MP, Yan J (2017)
574 Mechanotransmission and Mechanosensing of Human alpha-Actinin 1. *Cell Rep* 21: 2714-2723
575 Lemieux MG, Janzen D, Hwang R, Roldan J, Jarchum I, Knecht DA (2014) Visualization of the actin
576 cytoskeleton: different F-actin-binding probes tell different stories. *Cytoskeleton (Hoboken)* 71: 157-
577 169
578 Letort G, Ennomani H, Gressin L, Thery M, Blanchoin L (2015) Dynamic reorganization of the actin
579 cytoskeleton. *F1000Res* 4
580 Liebschner D, Afonine PV, Baker ML, Bunkoczi G, Chen VB, Croll TI, Hintze B, Hung LW, Jain S, McCoy AJ *et*
581 *al* (2019) Macromolecular structure determination using X-rays, neutrons and electrons: recent
582 developments in Phenix. *Acta Crystallogr D Struct Biol* 75: 861-877
583 Liu Y, Zhu W, Tan Y, Nakayasu ES, Staiger CJ, Luo ZQ (2017) A Legionella Effector Disrupts Host Cytoskeletal
584 Structure by Cleaving Actin. *PLoS Pathog* 13: e1006186
585 Machesky LM, Atkinson SJ, Ampe C, Vandekerckhove J, Pollard TD (1994) Purification of a cortical complex
586 containing two unconventional actins from Acanthamoeba by affinity chromatography on profilin-
587 agarose. *J Cell Biol* 127: 107-115

McDade JE, Shepard CC, Fraser DW, Tsai TR, Redus MA, Dowdle WR (1977) Legionnaires' disease: isolation of a bacterium and demonstration of its role in other respiratory disease. *N Engl J Med* 297: 1197-1203

McGhie EJ, Hayward RD, Koronakis V (2004) Control of actin turnover by a salmonella invasion protein. *Mol Cell* 13: 497-510

Melak M, Plessner M, Grosse R (2017) Actin visualization at a glance. *J Cell Sci* 130: 525-530

Meng EC, Goddard TD, Pettersen EF, Couch GS, Pearson ZJ, Morris JH, Ferrin TE (2023) UCSF ChimeraX: Tools for structure building and analysis. *Protein Sci* 32: e4792

Mondino S, Schmidt S, Rolando M, Escoll P, Gomez-Valero L, Buchrieser C (2020) Legionnaires' Disease: State of the Art Knowledge of Pathogenesis Mechanisms of Legionella. *Annu Rev Pathol* 15: 439-466

Munsie LN, Caron N, Desmond CR, Truant R (2009) Lifeact cannot visualize some forms of stress-induced twisted F-actin. *Nat Methods* 6: 317

Namgoong S, Boczkowska M, Glista MJ, Winkelman JD, Rebowski G, Kovar DR, Dominguez R (2011) Mechanism of actin filament nucleation by Vibrio VopL and implications for tandem W domain nucleation. *Nat Struct Mol Biol* 18: 1060-1067

Oliva G, Sahr T, Buchrieser C (2018) The Life Cycle of L. pneumophila: Cellular Differentiation Is Linked to Virulence and Metabolism. *Front Cell Infect Microbiol* 8: 3

Omotade TO, Roy CR (2020) Legionella pneumophila Excludes Autophagy Adaptors from the Ubiquitin-Labeled Vacuole in Which It Resides. *Infect Immun* 88

Pan ZN, Lu Y, Tang F, Pan MH, Wan X, Lan M, Zhang Y, Sun SC (2019) RAB8A GTPase regulates spindle migration and Golgi apparatus distribution via ROCK-mediated actin assembly in mouse oocyte meiosisdagger. *Biol Reprod* 100: 711-720

Pardee JD, Spudich JA (1982) Purification of muscle actin. *Methods Enzymol* 85 Pt B: 164-181

Pettersen EF, Goddard TD, Huang CC, Meng EC, Couch GS, Croll TI, Morris JH, Ferrin TE (2021) UCSF ChimeraX: Structure visualization for researchers, educators, and developers. *Protein Sci* 30: 70-82

Pizarro-Cerda J, Chorev DS, Geiger B, Cossart P (2017) The Diverse Family of Arp2/3 Complexes. *Trends Cell Biol* 27: 93-100

Pollard TD (2016) Actin and Actin-Binding Proteins. *Cold Spring Harb Perspect Biol* 8

Prashar A, Ortiz ME, Lucarelli S, Barker E, Tabatabeiyazdi Z, Shamoun F, Raju D, Antonescu C, Guyard C, Terebiznik MR (2018) Small Rho GTPases and the Effector VipA Mediate the Invasion of Epithelial Cells by Filamentous Legionella pneumophila. *Front Cell Infect Microbiol* 8: 133

Price CTD, Abu Kwaik Y (2021) Evolution and Adaptation of Legionella pneumophila to Manipulate the Ubiquitination Machinery of Its Amoebae and Mammalian Hosts. *Biomolecules* 11

Punjani A, Rubinstein JL, Fleet DJ, Brubaker MA (2017) cryoSPARC: algorithms for rapid unsupervised cryo-EM structure determination. *Nat Methods* 14: 290-296

Ribeiro Ede A, Jr., Pinotsis N, Ghisleni A, Salmazo A, Konarev PV, Kostan J, Sjoblom B, Schreiner C, Polyansky AA, Gkougkoulia EA *et al* (2014) The structure and regulation of human muscle alpha-actinin. *Cell* 159: 1447-1460

Riedl J, Crevenna AH, Kessenbrock K, Yu JH, Neukirchen D, Bista M, Bradke F, Jenne D, Holak TA, Werb Z *et al* (2008) Lifeact: a versatile marker to visualize F-actin. *Nat Methods* 5: 605-607

Satchell KJF (2015) Multifunctional-autoprocessing repeats-in-toxin (MARTX) Toxins of Vibrios. *Microbiol Spectr* 3

Schneider CA, Rasband WS, Eliceiri KW (2012) NIH Image to ImageJ: 25 years of image analysis. *Nat Methods* 9: 671-675

Swart AL, Hilbi H (2020) Phosphoinositides and the Fate of Legionella in Phagocytes. *Front Immunol* 11: 25

Tanaka K, Takeda S, Mitsuoka K, Oda T, Kimura-Sakiyama C, Maeda Y, Narita A (2018) Structural basis for cofilin binding and actin filament disassembly. *Nat Commun* 9: 1860

636 Thomas DR, Newton P, Lau N, Newton HJ (2020) Interfering with Autophagy: The Opposing Strategies
637 Deployed by Legionella pneumophila and Coxiella burnetii Effector Proteins. *Front Cell Infect*
638 *Microbiol* 10: 599762
639 Tomaskovic I, Gonzalez A, Dikic I (2022) Ubiquitin and Legionella: From bench to bedside. *Semin Cell Dev*
640 *Biol* 132: 230-241
641 Toulabi L, Wu X, Cheng Y, Mao Y (2013) Identification and structural characterization of a Legionella
642 phosphoinositide phosphatase. *J Biol Chem* 288: 24518-24527
643 Van Troys M, Vandekerckhove J, Ampe C (1999) Structural modules in actin-binding proteins: towards a
644 new classification. *Biochim Biophys Acta* 1448: 323-348
645 Vigorito E, Billadeu DD, Savoy D, McAdam S, Doody G, Fort P, Turner M (2003) RhoG regulates gene
646 expression and the actin cytoskeleton in lymphocytes. *Oncogene* 22: 330-342
647 von der Ecken J, Muller M, Lehman W, Manstein DJ, Penczek PA, Raunser S (2015) Structure of the F-actin-
648 tropomyosin complex. *Nature* 519: 114-117
649 Wan M, Minelli ME, Zhao Q, Marshall S, Yu H, Smolka M, Mao Y (2024) Phosphoribosyl modification of
650 poly-ubiquitin chains at the Legionella-containing vacuole prohibiting autophagy adaptor recognition.
651 *Nat Commun* 15: 7481
652 Wang JC, Lee JY, Christian S, Dang-Lawson M, Pritchard C, Freeman SA, Gold MR (2017) The Rap1-cofilin-
653 1 pathway coordinates actin reorganization and MTOC polarization at the B cell immune synapse. *J*
654 *Cell Sci* 130: 1094-1109
655 Xu Y, Ding K, Peng T (2024) Chemical Proteomics Reveals N(epsilon)-Fatty-Acylation of Septins by Rho
656 Inactivation Domain (RID) of the Vibrio MARTX Toxin to Alter Septin Localization and Organization.
657 *Mol Cell Proteomics* 23: 100730
658 Yin HL, Stossel TP (1979) Control of cytoplasmic actin gel-sol transformation by gelsolin, a calcium-
659 dependent regulatory protein. *Nature* 281: 583-586
660 Yu R, Ono S (2006) Dual roles of tropomyosin as an F-actin stabilizer and a regulator of muscle contraction
661 in Caenorhabditis elegans body wall muscle. *Cell Motil Cytoskeleton* 63: 659-672
662 Zago G, Biondini M, Camonis J, Parrini MC (2019) A family affair: A Ral-exocyst-centered network links Ras,
663 Rac, Rho signaling to control cell migration. *Small GTPases* 10: 323-330
664 Zahm JA, Padrick SB, Chen Z, Pak CW, Yunus AA, Henry L, Tomchick DR, Chen Z, Rosen MK (2013) The
665 bacterial effector VopL organizes actin into filament-like structures. *Cell* 155: 423-434
666 Zhang Q, Wan M, Mao Y (2023) Membrane-dependent actin polymerization mediated by the Legionella
667 pneumophila effector protein MavH. *bioRxiv*
668 Zhou Y, Huang C, Yin L, Wan M, Wang X, Li L, Liu Y, Wang Z, Fu P, Zhang N *et al* (2017) N(epsilon)-Fatty
669 acylation of Rho GTPases by a MARTX toxin effector. *Science* 358: 528-531
670 Zhu W, Banga S, Tan Y, Zheng C, Stephenson R, Gately J, Luo ZQ (2011) Comprehensive identification of
671 protein substrates of the Dot/Icm type IV transporter of Legionella pneumophila. *PLoS One* 6: e17638

672

673 **Figure legends**

674

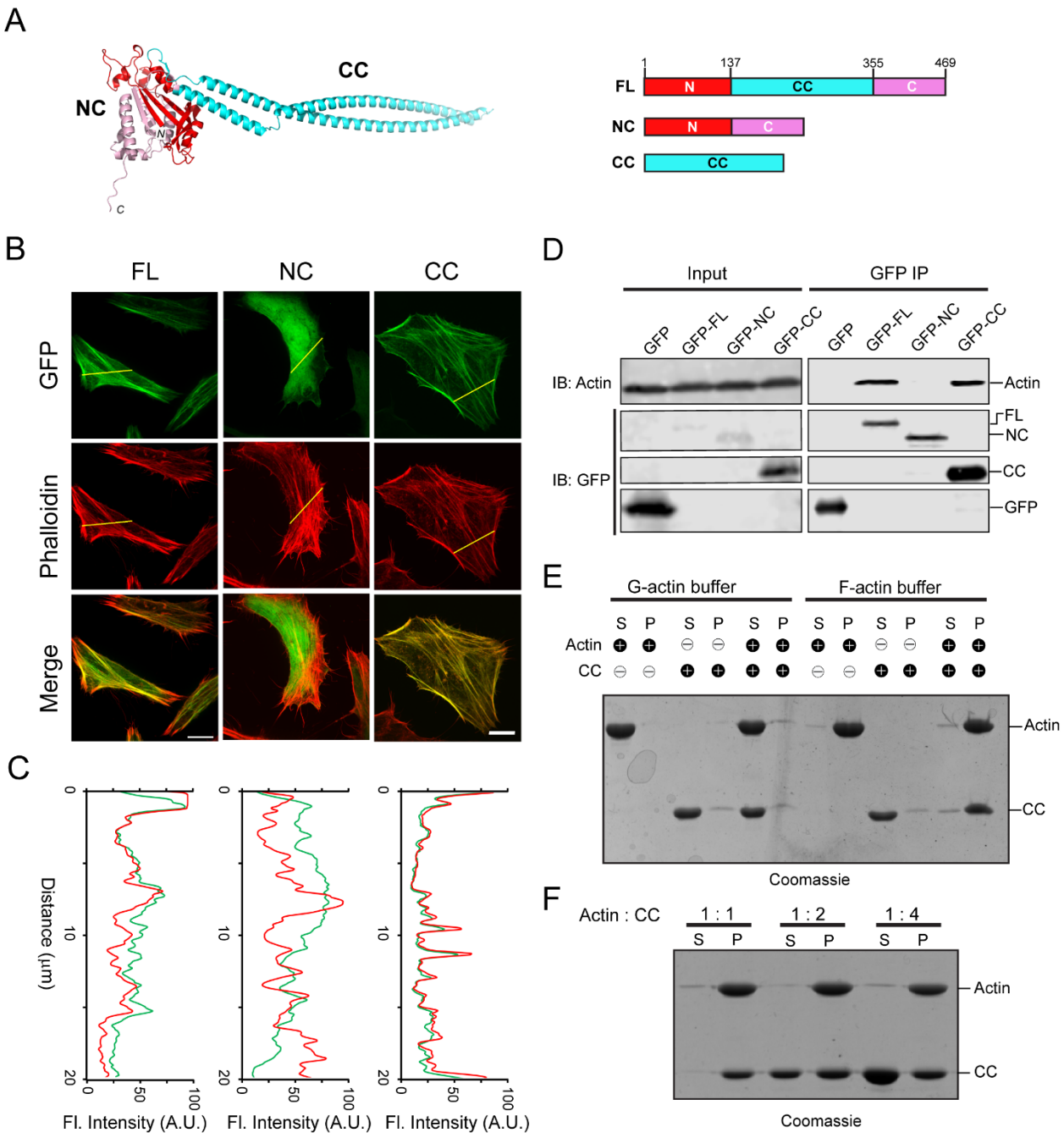

675

676 **Figure 1. Identification of LFat1 (lpg1387) as an F-actin binding effector**. (A) AlphaFold-

677 prediction structure of Lfat1 (Left) and domain architecture of Lfat1 (Right) with the N-terminal

678 domain shown in red, the C-terminal domain in pink, and the central coiled-coil domain in cyan.

679 FL: Full-length, NC: NC domain, CC: Coiled-coil domain, respectively. (B) Cellular localization
680 of Lfat1-FL, -NC, or -CC as determined by fluorescence microscopy. HeLa cells transiently
681 expressing GFP-fused Lfat1-FL, -NC, or -CC were fixed and stained with phalloidin. Scale bar =
682 10 μm. (C) Colocalization was determined by fluorescence intensity line scan along the yellow
683 line shown in (B). Red = F-actin, Green = GFP. (D) Co-immunoprecipitation to determine
684 interaction of Lfat1 with actin. HEK293T cells transiently expressing either GFP-empty vector, -
685 Lfat1 FL, -Lfat1 NC, or -Lfat1 CC were lysed, and cell lysates were immunoprecipitated using
686 anti-GFP nanobeads. The IP samples were analyzed with SDS-PAGE followed by immunoblot
687 against GFP and actin. (E) Co-sedimentation assay to determine direct interaction between Lfat1
688 CC with F-actin. Purified G-actin, CC, or G-actin plus CC was incubated either in G-actin buffer
689 or F-actin polymerization buffer, then ultra-centrifuged to separate supernatant from pellet,
690 followed by analysis via SDS-PAGE. S: supernatant, P: pellet. (F) Binding stoichiometry between
691 Lfat1 CC and actin as determined by co-sedimentation assay.
692
693

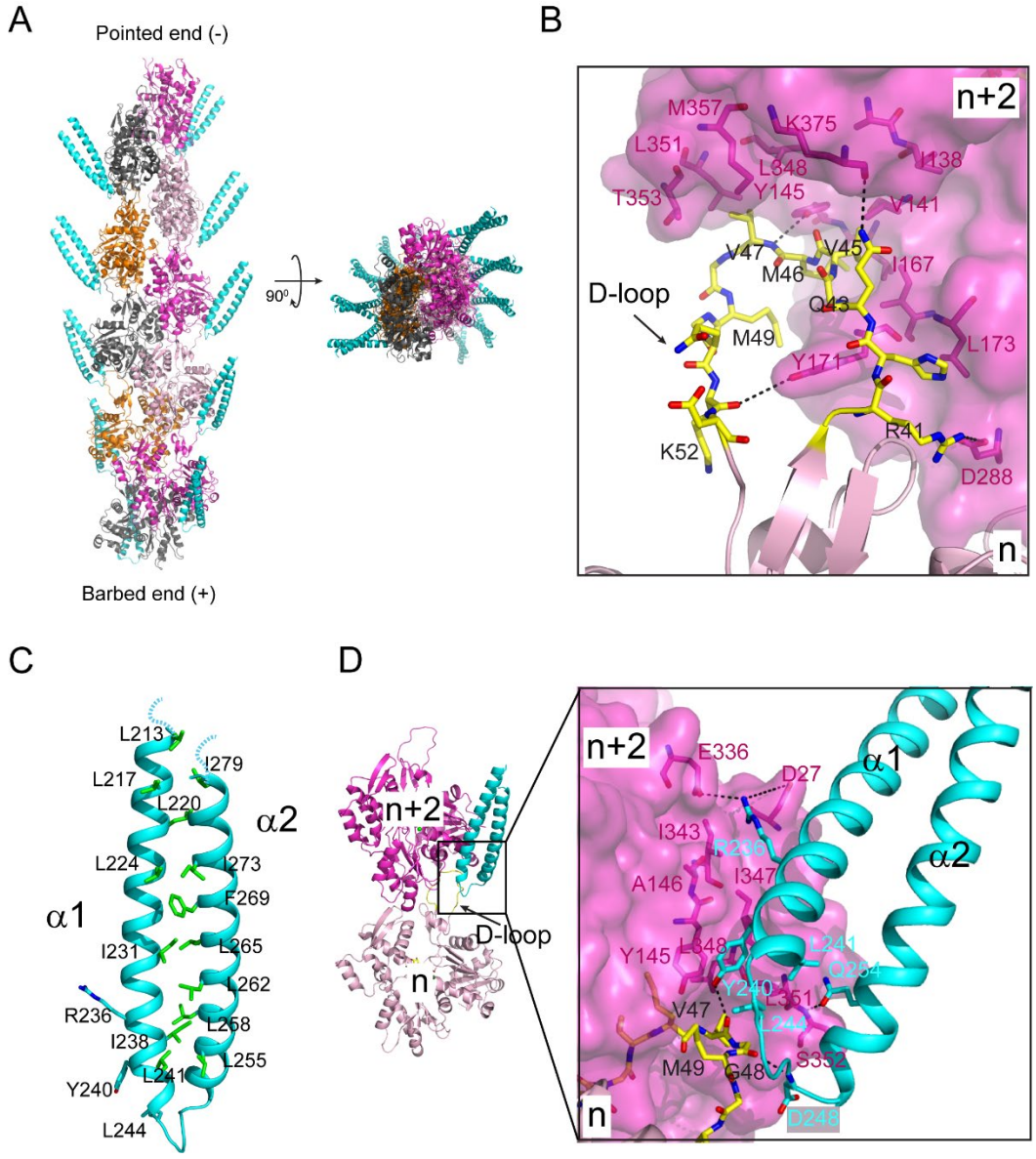

Figure 2. Cryo-EM structure of the Lfat1 ABD in complex with F-actin. (A) Cryo-EM structure of the F-actin-Lfat1 ABD complex. Left: side view of the structure positioned with the pointed end (-) up and barbed end (+) down. The visible part of ABD is colored in cyan. Right: Top view of the complex. (B) The D-loop conformation and its interactions in the hydrophobic cleft of the n+2nd actin monomer. (C) Ribbon diagram of the distal portion of the Lfat1 coiled-coil domain. The two α-helices are zipped together through extensive hydrophobic interactions

702 contributed mainly by leucine and iso-leucine residues (shown in sticks). (D) Structural
703 representation of the interaction between the ABD domain of Lfat1 and F-actin. Inset: Extensive
704 hydrophobic, hydrogen bonding, and electrostatic interactions were observed between the Lfat1
705 ABD domain and the two adjacent actin monomers (details see in the text).
706

707

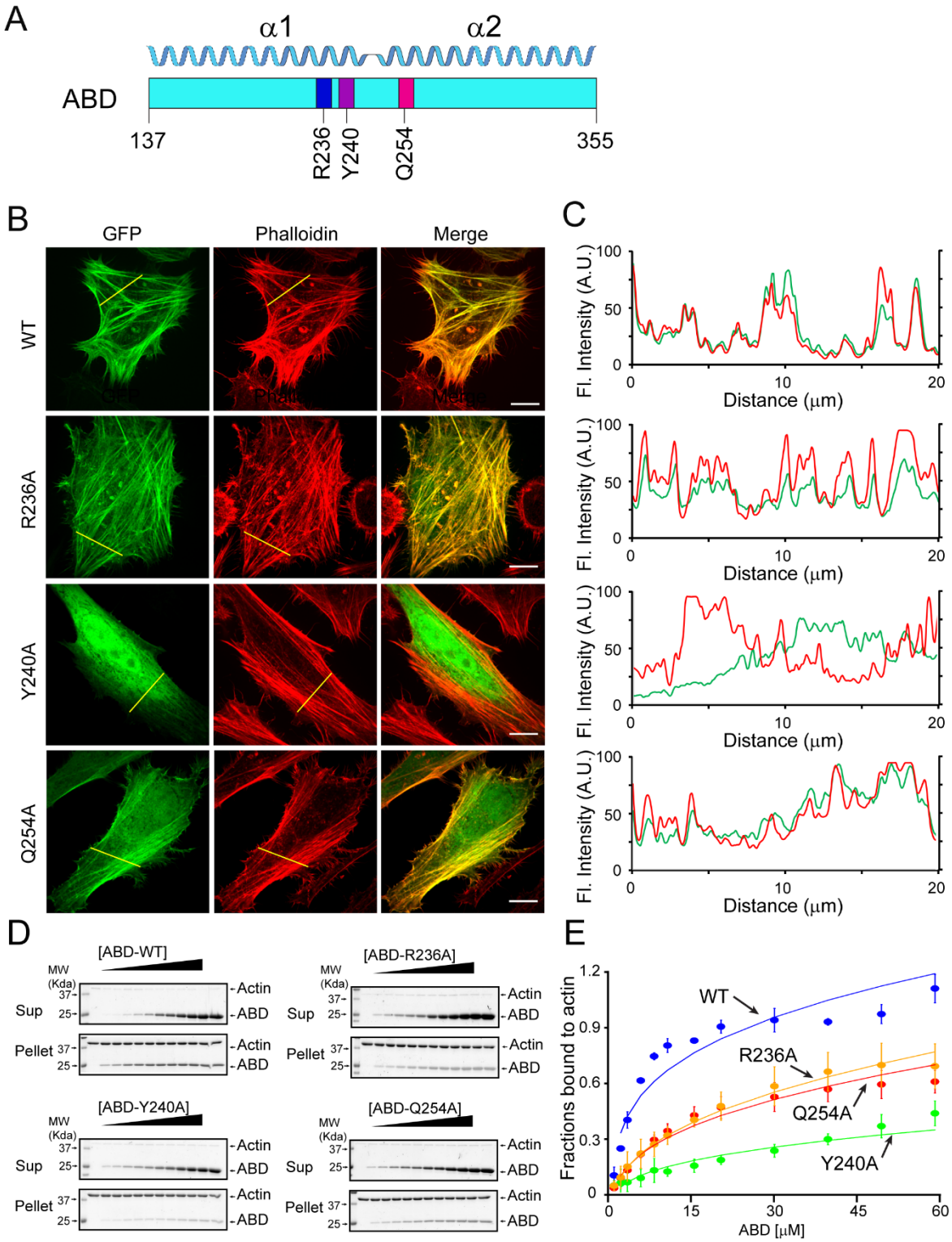
A
α1
α2
ABD
137
R236
Y240
Q254
355
B
GFP
Phalloidin
Merge
WT
R236A
Y240A
Q254A
C
Fl. Intensity (A.U.)
Distance (μm)
D
[ABD-WT]
[ABD-R236A]
[ABD-Y240A]
[ABD-Q254A]
MW (Kda)
Sup
Pellet
Actin
ABD
E
Fractions bound to actin
ABD [μM]
WT
R236A
Q254A
Y240A

708

709 **Figure 3. Validation of key Lfat1 ABD residues in their contributions to F-actin interactions..**
710 (A) Schematic diagram of the Lfat1 ABD domain. Three key residues (R236, Y240, and Q254)
711 involved in actin binding are labeled. **(**B and C) F-actin localization analysis of indicated ABD
712 mutants. GFP-Lfat1 WT, R236A, Y240A, or Q254A mutant was transiently expressed in HeLa
713 cells followed by fixation and staining with phalloidin. Fluorescence images were taken by a
714 confocal microscope and analyzed using Line scan along the indicated yellow lines. Scale bar =
715 10 μm. (D) Co-sedimentation assay of F-actin with WT and mutant Lfat1 ABD. Increasing
716 amounts (0 to 60 μM) of recombinant WT or mutant ABD proteins were incubated with a fixed
717 amount of actin. The samples were ultra-centrifugated after 30 min of room temperature incubation
718 in 1x actin polymerization buffer. The supernatant and pellet fractions were analyzed by SDS-
719 PAGE. (E) Quantitative analysis of the co-sedimentation titration data. The data point for each
720 concentration was averaged from three independent experiments. The error bar represents the
721 standard deviation.
722

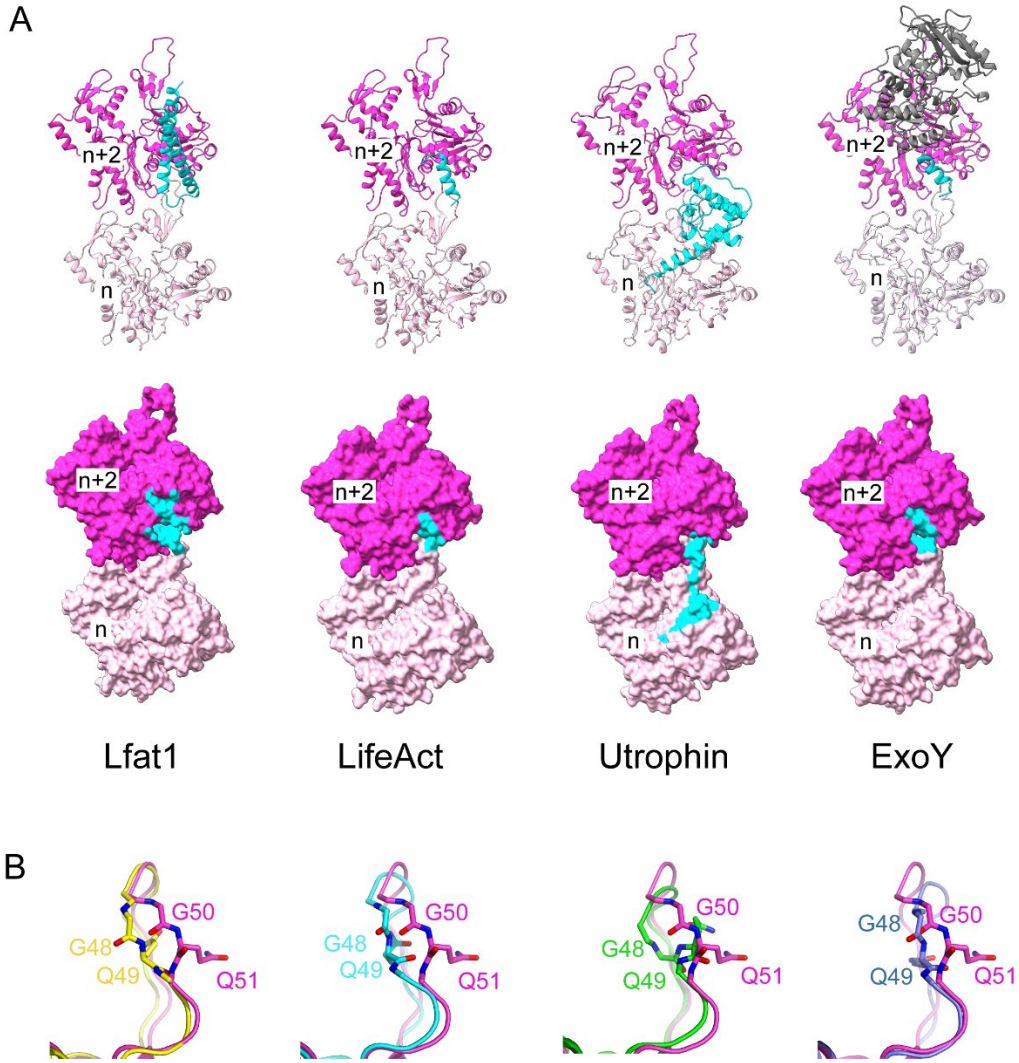

Figure 4. Structural comparison between Lfat1 and other ABD-F-actin complexes. (A) Ribbon diagram (Upper row) and surface representation (bottom row) of two adjacent actin monomers (purple and pink) bound with Lfat1 ABD, LifeAct (PDB ID: 7BTE), Utrophin (6M5G), and ExoY (7P1G). The region interfacing with each ABD is colored in cyan. (B) Structural comparison of the D-loop conformation in the Lfat1 ABD-F-actin complex (purple) with the D-loop in other F-actin-ABD complexes. F-actin alone (yellow), LifeAct (cyan), Utrophin (green), and ExoY (navy blue). Two D-loop residues with the largest deviation of backbone dihedral angles (G50 and Q51) are shown in sticks.

733

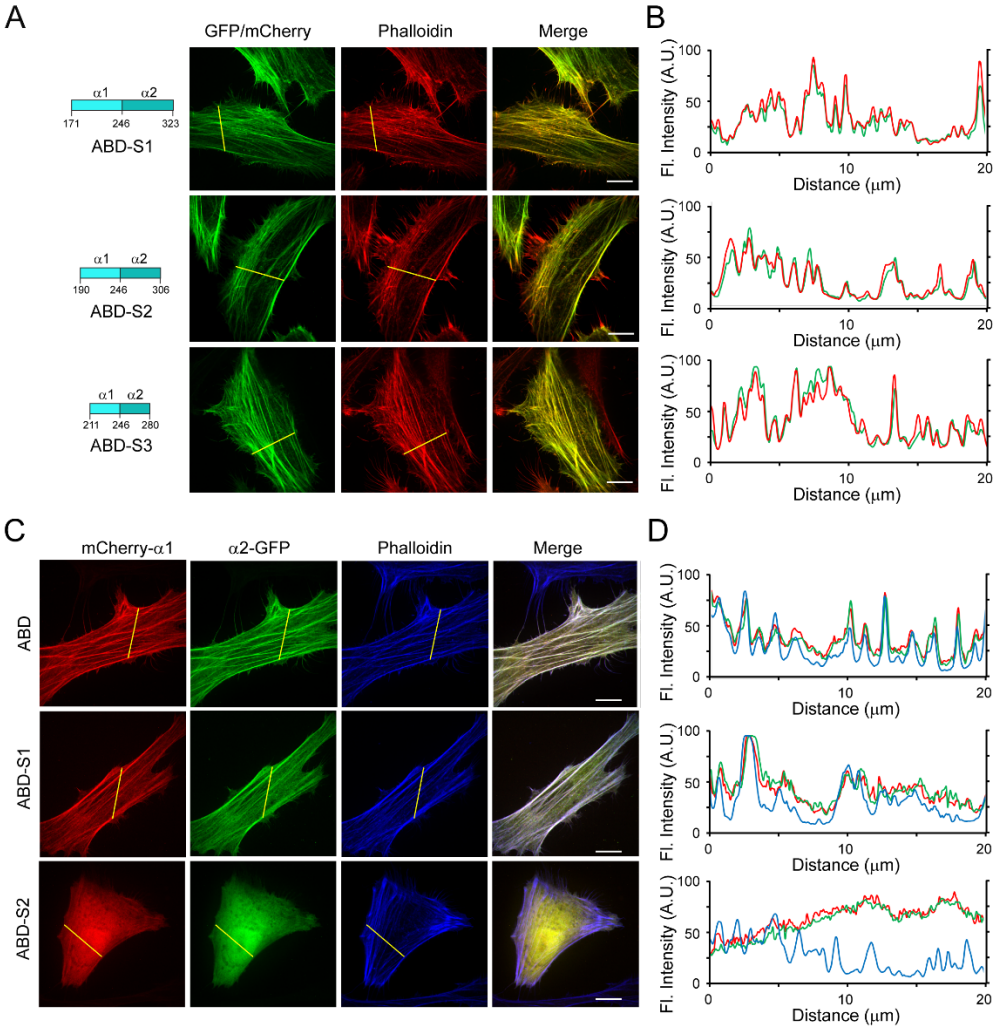

734

735 **Figure 5. Engineering Lfat1 ABD as an *in vivo* F-actin probe.** (A) Mapping the minimal actin-
736 binding domain of Lfat1. Schematic of shortened Lfat1ABD fragments used for F-actin binding
737 (Left). Representative fluorescence images of cells expressing indicated ABD fragments and
738 stained with rhodamine-phalloidin. (B) Line-scan analysis for the indicated ABD probes along the
739 yellow lines. (C) Representative fluorescence images of cells transiently transfected with plasmids
740 expressing separated alpha helixes (mCherry-α1 and α2-GFP) of ABD, ABD-S1, and ABD-S2.
741 The cells were fixed and stained with CF647-phalloidin. (D) Line-scan analysis of the images
742 shown in (C). Scale bar = 10 μm.

743

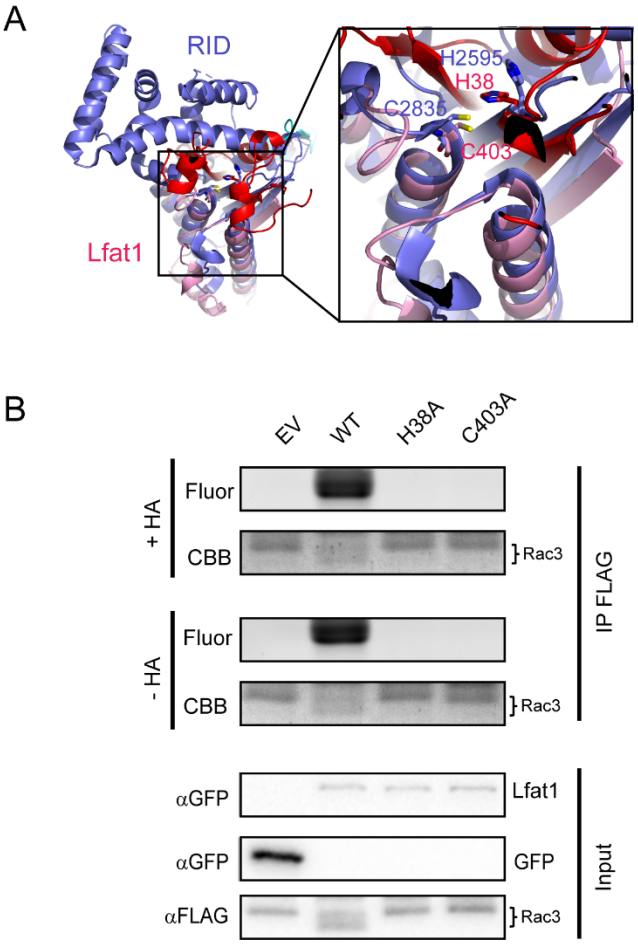

744

745 **Figure 6. Lfat1 is a lysine fatty acyltransferase that modifies eukaryotic small GTPases.** (A)
746 Ribbon representation of the *Vibrio vulnificus* RID (PDB ID: 5XN7) catalytic domain (purple)
747 superimposed with the AlphaFold-predicted NC-domain of Lfat1 (N-terminal domain in red, C-
748 terminal domain in pink). Inset: the catalytic pockets of the two proteins with conservation of the
749 catalytic histidine and cysteine between RID and Lfat1 shown in sticks. (B) Lfat1 catalyzes lysine
750 fatty acylation of Rac3. N-terminal Flag-tagged Rac3 was co-expressed with either GFP empty
751 vector (EV), GFP-Lfat1 WT, H38A, or C403A mutant in HEK293T cells for 24 hours. Flag-Rac3
752 was enriched using immunoprecipitation and subjected to Click chemistry. The samples were then
753 separated on SDS-PAGE and scanned for fluorescence signals.

754

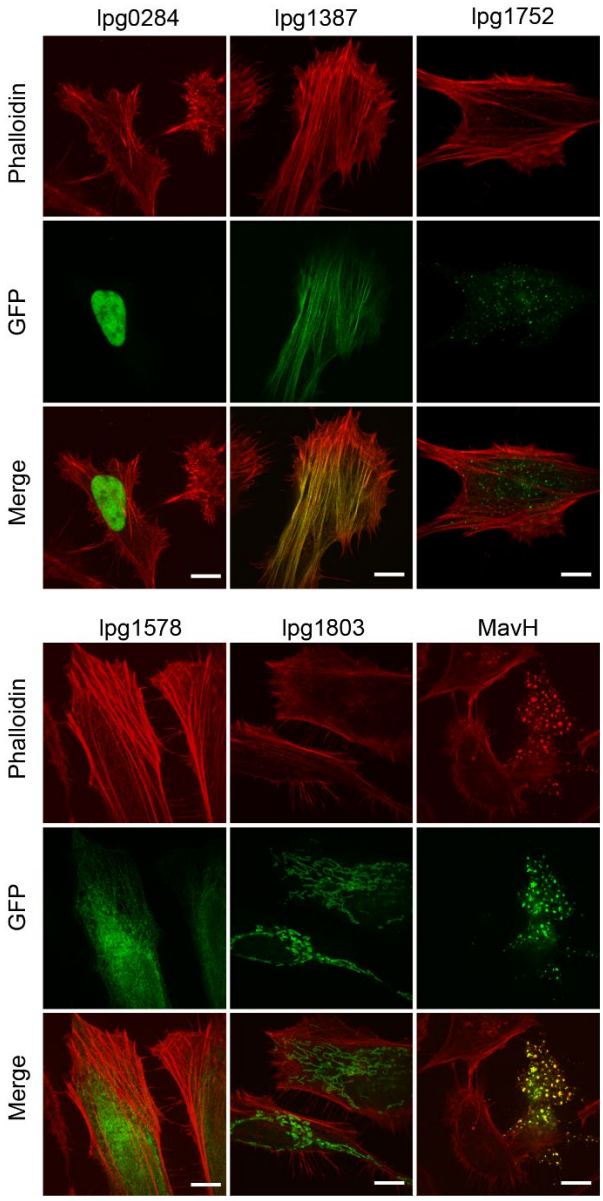

755

756 **Figure S1. Intracellular localization representative Legionella effectors.** Individual plasmid
757 from a library consisting of 315 GFP-tagged *Legionella pneumophila* effectors was transiently
758 expressed in HeLa cells followed by PFA fixation, stained with rhodamine-phalloidin, and
759 visualized by fluorescence microscopy. Images showing intracellular localization of several
760 representative effectors: lpg0284 (nuclear); lpg1387 and MavH (F-actin); lpg1578 (ER); and
761 lpg1803 (mitochondrial). Scale bar = 10 µm.

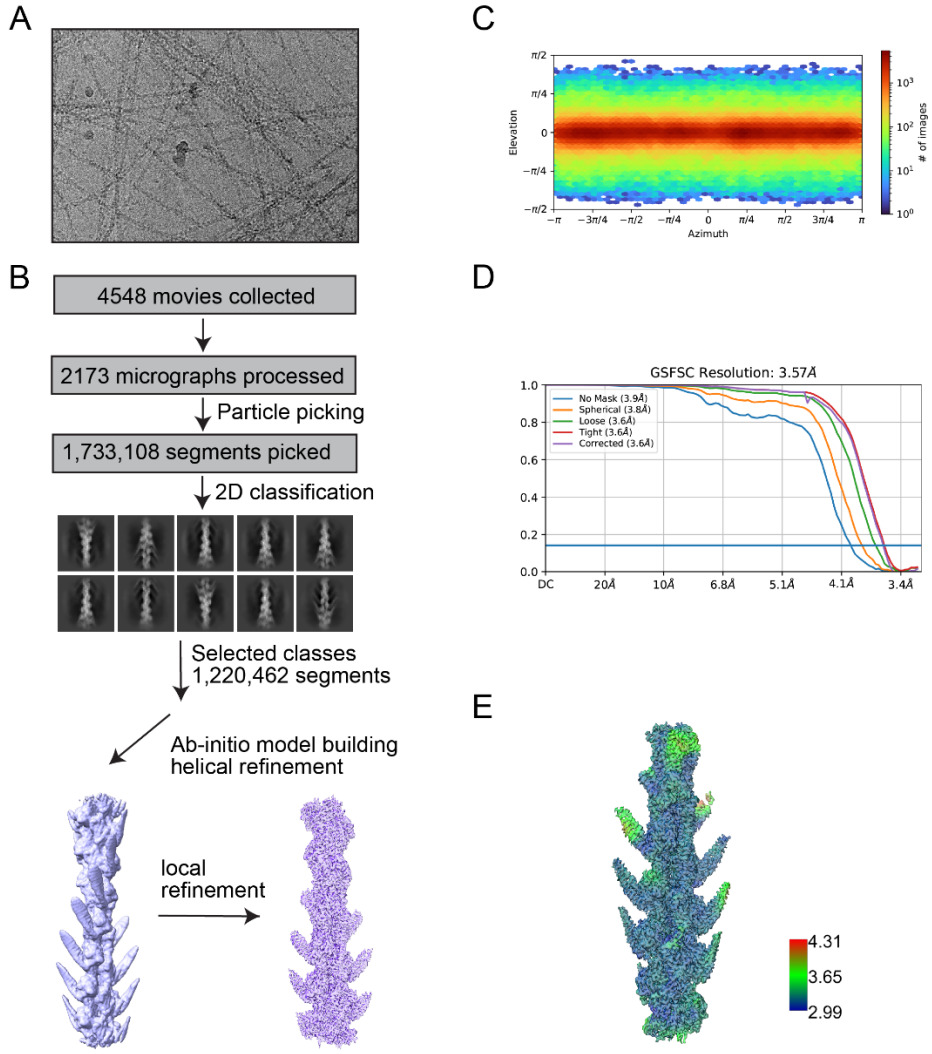

Figure S2. CryoEM data processing details of F-actin-Lfat1ABD complex. (A) Representative CryoEM micrograph of Lfat1ABD-F-actin complex. (B) Data-processing and structure determination workflow. Movies were collected at Talos Arctica electron microscope. Motion correction and patch CTF estimation were performed using CryoSPARC. Following manual curation, automatic filament tracer-based particle picking, and extraction, 1.2 million particles were 2-D classified and an ab initio model was built and refined using helical refinement until convergence. (C) Angular distribution of particles. (D) Resolution estimation by GSFSC. (E) Local resolution map of the final CryoEM map.

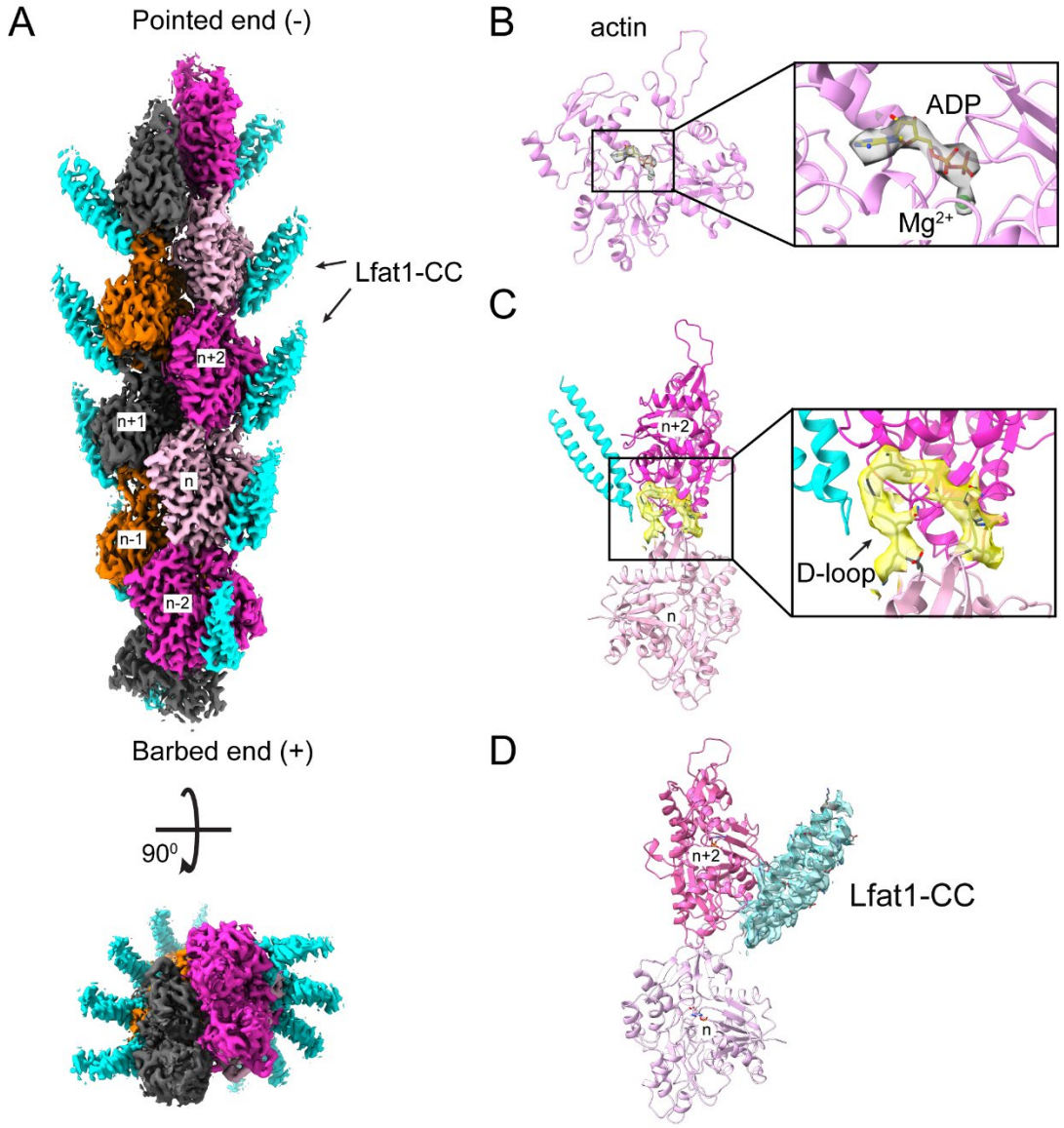

Figure S3. CryoEM maps of the F-actin-Lfat1ABD complex. (A) Final CryoEM density map of the complex. Top: Side view of the complex density map with the pointed end (-) up and barbed end (+) down. Lfat1 ABD is shown in cyan. Bottom: Top view of the complex density map. (B) The EM density map (grey) of ADP-Mg^{2+} at the ATP binding cleft of actin subunits. (C) The EM-map of actin D-loop (yellow). (D) The EM density map (cyan) of the distal region of the Lfat1 hairpin.

780

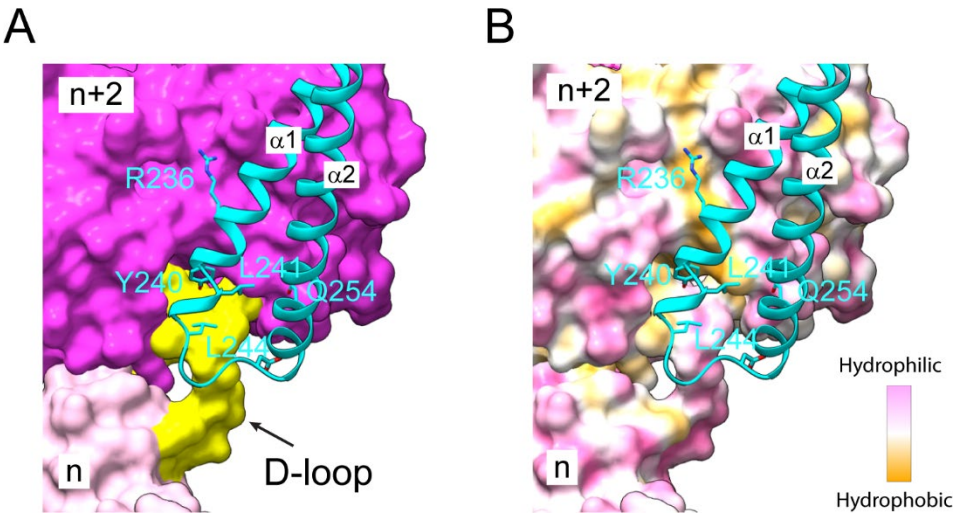

781

782 **Figure S4 The interface between Lfat1 ABD and F-actin.** (A) Surface representative of two
783 adjacent actin molecules (purple and pink) and the D-loop region of the nth actin molecule is
784 colored yellow. Lfat1 ABD is represented as a ribbon in cyan. Key residues involved in F-actin
785 interaction are shown in sticks. (B) The interface between Lfat1 ABD and F-actin at the same
786 orientation as in (A). The surface of the two actin molecules is colored based on hydrophobicity,
787 with hydrophobic areas in orange and hydrophobic regions in pink.

788

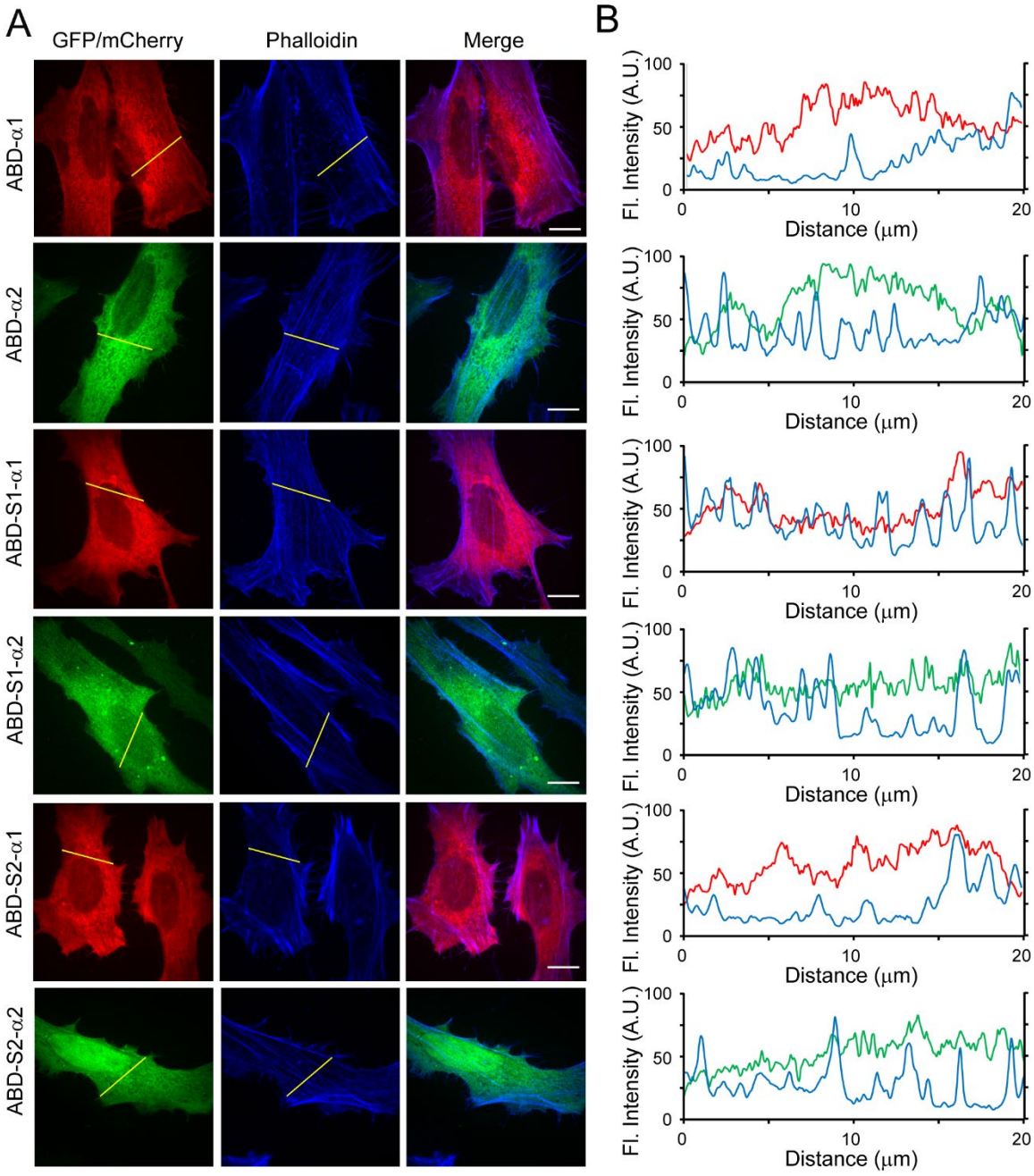

Figure S5. Intracellular localization of separated individual alpha helixes of the Lfat1 ABD. (A) Representative images of HeLa cells transiently expressing individual alpha-helixes from full-length and truncated Lfat1 ABD. Cells were fixed and stained with CF647-phalloidin. (B) Line-scan analysis of constructs tested in (A). Scale bar = 10 μm.

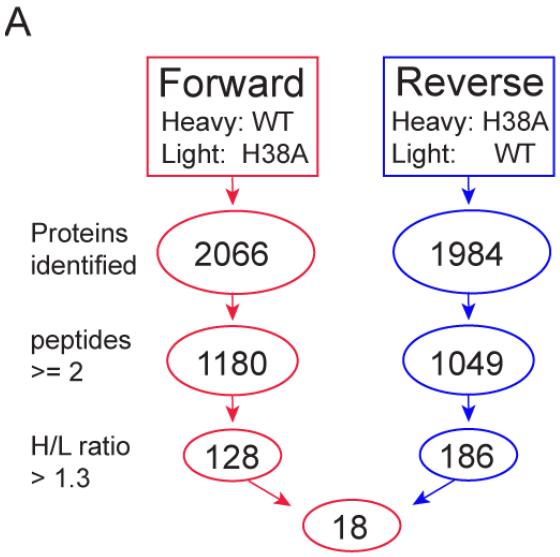

B

Protein Name	Forward H/L	Reverse H/L	annotation
RHEB	100	0.01	Small GTPase
ACBD3	100	0.513	Golgi biogenesis
PSMC5	100	0.742	Proteosome subunit
RAP1B	8.904	0.354	Small GTPase
ATP1B3	5.829	0.298	ATPase subunit
RAB13	4.486	0.444	Small GTPase
RAB8A	4.22	0.509	Small GTPase
RAB10	4.141	0.651	Small GTPase
YKT6	3.66	0.621	SNARE protein
RHOG	3.617	0.631	Small GTPase
TBC1D10B	2.438	0.251	RABGAP
RALB	1.96	0.641	Small GTPase
SEPTIN7	1.858	0.606	GTPase/Shigellosis
RALA	1.725	0.573	Small GTPase
NCAPG	1.619	0.622	Condensin Subunit
ATP1A1	1.505	0.765	ATPase subunit
SEPTIN11	1.454	0.01	GTPase/Shigellosis
CUL4B	1.427	0.789	E3 ligase

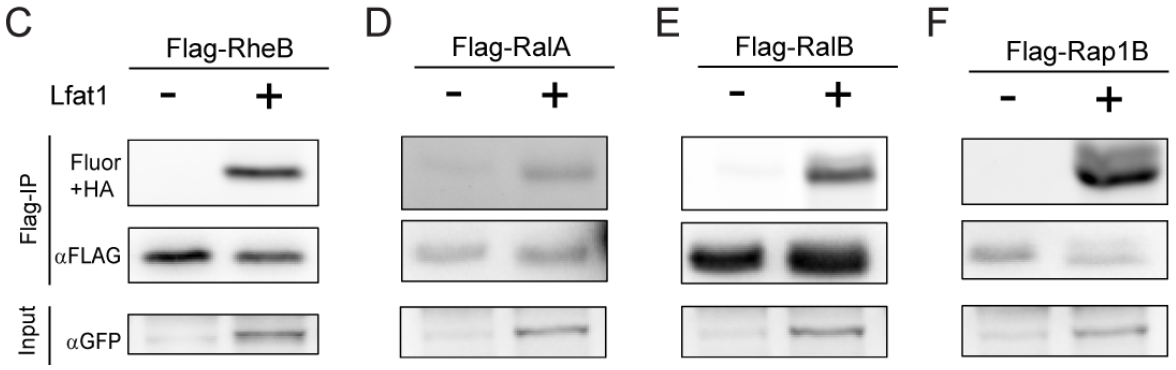

Figure S6. Identification of potential Lfat1 substrates by Click chemistry-coupled SILAC mass spectrometry. (A) Flow chart for selecting high-confidence substrate hits from the SILAC screen. (B) Top hits of potential Lfat1 substrates identified in this SILAC-MS experiment. (C) – (F) Click chemistry verification of some small GTPases selected from the top hit list. N-terminal Flag-tagged RheB, RalA, RalB, or Rap1B was co-expressed along with GFP-Lfat1 or GFP control in HEK293T cells followed by anti-Flag immunoprecipitation and Click chemistry conjugation reaction with an Azide-containing fluorophore. The samples were separated on SDS-PAGE and scanned for fluorescence signals.

Supplemental Table 1. CryoEM Data collection, refinement, and validation statistics.

Microscope	FEI Talos Artica
Voltage (keV)	200
Defocus range (um)	-0.4 to -3.0
Camera	K3 direct electron detector
Pixel size (Å)	0.833
Total electron dose (e/Å2)	40.68
Exposure time (seconds)	1.23
Frames per movie	50
Number of images	4548
3-D refinement statistics and helical symmetry	
Total number of particles	1,220,462
Resolution (Å)	3.58
Helical twist	-167
Rise	28
Model composition and validation	
Non-hydrogen atoms	34,740
Protein residues	4390
Ligands	10Mg, 10ADP
RMSD	
Bond lengths(Å)	0.25
Bond angles (°)	0.5
B-factor (Å2) Protein	58.87
B-factor (Å2) Ligand (ADP)	56.6
MolProbity Score	1.9
Clashscore	5
Ramachandran plot:-Favored	95
Allowed	5
Outlier	0
PDB ID	8VAA
EMDB Code	43087

Supplemental Table 2. Primers used in this study.

	Construct	Forward primer	reverse primer
1	Lfat1-NC	ATCAAAAGCCGTGATtttactgaaggaaggcaacc	ATCACGGCTTTTGATttcagaaatcatatcttcttcatgag
2	Lfat1-ABD	GGGGATGGATCCatggattcggtaacagcaatgactattatc	GACCTCGAGTTAatcacggcttttgatgaattg
3	ABD-R236A	caaattacagctacagagGCGactataaatttatttaaat	atttaaataatttatagtCGCctctgtagctgtaatttg
4	ABD-Y240A	gagagaactataaatgctttaaataaactgaaa	tttcagtttatttaaagcatttatagttctctc
5	ABD-Q254A	cctaaaaccaaaacagctttgattgagcttact	agtaagctcaatcaaagctgttttggtttagg
6	ABD-S1	GGGGGGGGGATCCttggaagtcaacttggagcaaag	CCCCCCCCTCGAGCTAattgattttaatatccagctttttcaaatcttc
7	ABD-S2	GGGGGGGGGATCCttggaaaaagatgaattgattaaacaacag	CCCCCCCCTCGAGCTAaagctcaatctgttgcagtttc
8	ABD-S3	GGGGGGGGGATCCaaagatttaaaggggcaattagc	CCCCCCCCTCGAGGGCTAgcttatctcatgttgagaatttattg
9	ABD-α1	caaattacagctacagagGCGactataaatttatttaaat	CCCCCCCCTCGAGCTAatttttcagtttatttaaataatttatagttctc
10	ABD-S1-α1	GGGGGGGGGATCCttggaagtcaacttggagcaaag	CCCCCCCCTCGAGCTAatttttcagtttatttaaataatttatagttctc
11	ABD-S2-α1	GGGGGGGGGATCCATGttaaccaattcttaccaaaccc	CCCCCCCCTCGAGCTAatttttcagtttatttaaataatttatagttctc
12	ABD-S3-α1	GGGGGGGGGATCCaaagatttaaaggggcaattagc	CCCCCCCCTCGAGCTAatttttcagtttatttaaataatttatagttctc
13	ABD-α2	GGGGGGGGGATCCGCCACCATGGTGcctgatcctaaaaccaaaacac	CCCCCCCCTCGAGGGatcacggcttttgatgaattg
14	ABD-S1-α2	GGGGGGGGGATCCGCCACCATGGTGcctgatcctaaaaccaaaacac	CCCCCCCCTCGAGAAattgatttaatatccagctttttcaaatcttc
15	ABD-S2-α2	GGGGGGGGGATCCGCCACCATGGTGcctgatcctaaaaccaaaacac	CCCCCCCCTCGAGGGaagctcaatctgttgcagtttc
16	ABD-S3-α2	GGGGGGGGGATCCGCCACCATGGTGcctgatcctaaaaccaaaacac	CCCCCCCCTCGAGGGgcttatctcatgttgagaatttattg
17	LFat1-H38A	gataaaggggaaaatgtaggaGCCgttaatttttactatagaaattg	caatttctatagtaaaattaacGGCtcctacattttccccttttatc
18	LFat1-C403A	ctattcatttctttttaataacGCTgccagtagtgctaaacgttg	caacgtttagcactactggcAGCgttattaaaaagaaatgaatag

Supplemental Table 3. Constructs used in this study.

	Description	ID	Source
1	Lfat1 FL in pET28a His-SUMO	YM2526	This study
2	Lfat1-Full length in pEGFPC1	YM2527	This study
3	Lfat1-NC in pEGFPC1	YM2528	This study
4	Lfat1-ABD in pEGFPC1	YM2529	This study
5	Lfat1-ABD in pET28a His-SUMO	YM2530	This study
6	ABD- R236A in pEGFPC1	YM2531	This study
7	ABD-Y240A in pEGFPC1	YM2532	This study
8	ABD-Q254A in pEGFPC1	YM2533	This study
9	ABD- R236A in pET28a His-SUMO	YM2534	This study
10	ABD-Y240A in pET28a His-SUMO	YM2535	This study
11	ABD-Q254A in pET28a His-SUMO	YM2536	This study
12	ABD-S1 in pEGFPC1	YM2537	This study
13	ABD-S1 in pEGFPC1	YM2538	This study
14	ABD-S1 in pEGFPC1	YM2539	This study
15	ABD-α1 in pmCherryC1	YM2540	This study
16	ABD-S1-α1 in pmCherryC1	YM2541	This study
17	ABD-S2-α1 in pmCherryC1	YM2542	This study
18	ABD-S3-α1 in pmCherryC1	YM2543	This study
19	ABD-α2 in pEGFPC1	YM2544	This study
20	ABD-S1-α2 in pEGFPC1	YM2545	This study
21	ABD-S2-α2 in pEGFPC1	YM2546	This study

22	ABD-S3-α2 in pEGFPC1	YM2547	This study
23	LFat1-H38A in pEGFPC1	YM2548	This study
24	LFat1-C403A in pEGFPC1	YM2549	This study